

## RESEARCH ARTICLE

10.1002/2017JD027796

## Key Points:

- This study examines the local and large-scale forcing of Antarctic continental temperature record through observation and modeling experiments
- We attribute ~60% of the warming at the Esperanza station directly to the foehn effect rather than the advection of warm air from midlatitudes
- At the same time, the widespread foehn episode was triggered by the large-scale moisture advection associated with an atmospheric river

## Supporting Information:

- Supporting Information S1
- Figures S1–S12

## Correspondence to:

D. Bozkurt,  
dbozkurt@dgf.uchile.cl

## Citation:

Bozkurt, D., Rondanelli, R., Marin, J. C., & Garreaud, R. (2018). Foehn event triggered by an atmospheric river underlies record-setting temperature along continental Antarctica. *Journal of Geophysical Research: Atmospheres*, 123, 3871–3892. <https://doi.org/10.1002/2017JD027796>

Received 27 SEP 2017

Accepted 14 FEB 2018

Accepted article online 23 FEB 2018

Published online 21 APR 2018

## Foehn Event Triggered by an Atmospheric River Underlies Record-Setting Temperature Along Continental Antarctica

D. Bozkurt<sup>1</sup> , R. Rondanelli<sup>1,2</sup> , J. C. Marin<sup>3,4</sup> , and R. Garreaud<sup>1,2</sup> 

<sup>1</sup>Center for Climate and Resilience Research, University of Chile, Santiago, Chile, <sup>2</sup>Department of Geophysics, University of Chile, Santiago, Chile, <sup>3</sup>Department of Meteorology, University of Valparaiso, Valparaiso, Chile, <sup>4</sup>Interdisciplinary Center for Atmospheric and Astro-statistical Studies, University of Valparaiso, Valparaiso, Chile

**Abstract** A record-setting temperature of 17.5°C occurred on 24 March 2015 at the Esperanza station located near the northern tip of the Antarctic Peninsula (AP). We studied the event using surface station data, satellite imagery, reanalysis data, and numerical simulations. The Moderate Resolution Imaging Spectroradiometer Antarctic Ice Shelf Image Archive provides clear evidence for disintegration and advection of sea ice, as well as the formation of melt ponds on the ice sheet surface at the base of the AP mountain range. A deep low-pressure center over the Amundsen-Bellingshausen Sea and a blocking ridge over the southeast Pacific provided favorable conditions for the development of an atmospheric river with a northwest-southeast orientation, directing warm and moist air toward the AP, and triggering a widespread foehn episode. A control simulation using a regional climate model shows the existence of local topographically induced warming along the northern tip of the AP (~60% of the full temperature signal) and the central part of the eastern AP (>90% of the full temperature signal) with respect to a simulation without topography. These modeling results suggest that more than half of the warming experienced at Esperanza can be attributed to the foehn effect (a local process), rather than to the large-scale advection of warm air from the midlatitudes. Nevertheless, the local foehn effect also has a large-scale advection component, since the atmospheric river provides water vapor for orographic precipitation enhancement and latent heat release, which makes it difficult to completely disentangle the role of local versus large-scale processes in explaining the extreme event.

### 1. Introduction

The Antarctic Peninsula (AP), spanning ~63°S to 70°S, consists of a narrow and rugged NE-SW oriented mountain chain, with complex topography averaging 70 km in width and 1,500 m in height (King & Turner, 2009). The AP, featuring several islands and archipelagos, is the northward extension of the Antarctic continent toward South America. The AP is heavily ice covered, with a large ice sheet extending over the terrestrial surface and Larsen C ice shelf along the coastal zone of the AP (Oliva et al., 2017) (see Figure 1). Covering about 80% of the landmass, the contemporary ice cover on the AP averages 500 m in thickness, and the Larsen Ice Shelf constitutes a large part of the eastern margin of the AP, fed by ice flows from a number of outlets and valley glaciers (Cofaigh et al., 2014; Pritchard & Vaughan, 2007).

The climate of the AP is under the influence of strong westerlies, as well as midlatitude baroclinic systems. For instance, the Amundsen-Bellingshausen Sea low brings relatively warm and moist midlatitude air masses toward the AP, while a climatological low-pressure center in the Weddel Sea brings cold, dry air toward the eastern part of the peninsula (King & Turner, 2009; Oliva et al., 2017). The NE-SW mountain range acts as an orographic barrier to westerly winds. Therefore, the AP comprises two distinct climatological regions: a mild, maritime climate along the western coastline and a cold, continental climate along the eastern coastline. Due to the large oceanic influence, the AP, constituting the northernmost tip of Antarctica, has the mildest climate of the continent. For instance, summer mean temperatures range from 0.5°C to 1.2°C and –2.5°C to 0.2°C along the west and east coasts, respectively (King & Turner, 2009). In addition, the contrasting wind regimes on each side of the AP lead to 5–10°C differences in annual mean surface temperatures at similar latitudes across the mountain range (Cape et al., 2015; Cook & Vaughan, 2010; King & Turner, 2009).

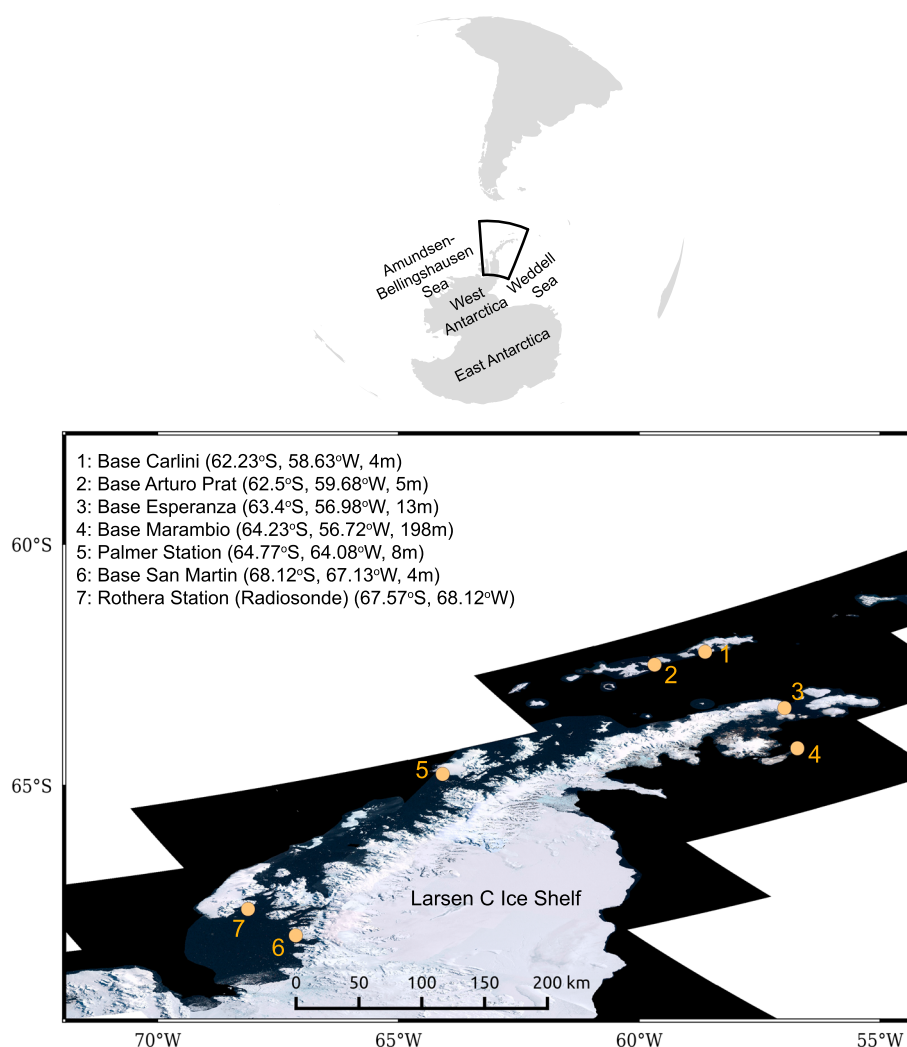


**Figure 1.** The Antarctic Peninsula on a digital elevation map derived from the Landsat Image Mosaic of Antarctica (Bindschadler et al., 2008). The dots show the location of meteorological observations used in this study.

West Antarctica, particularly the AP, has also recently been a site of remarkable temperature change, with a long-term warming trend in near-surface temperature observed over the last 50 years (Cape et al., 2015; Marshall et al., 2006; Turner et al., 2016), coupled with a shorter cooling trend since 2002 (e.g., Carrasco, 2013; Oliva et al., 2017; Turner et al., 2016). The long-term warming trend is accompanied by changes in the cryosphere and ecosystem processes. For instance, glacier retreats and large ice mass losses have occurred in recent years (e.g., Cook et al., 2005; Rignot et al., 2004; Scambos et al., 2004), alongside changes in terrestrial biology (e.g., Convey & Smith, 2006) and marine ecosystems (e.g., Cape et al., 2014; Montes-Hugo et al., 2009; Schofield et al., 2010). Recent changes in large-scale circulation patterns (e.g., Southern Annular Mode) and associated strengthening of westerly marine air advection are thought to be the main drivers of the long-term warming trend in the AP (e.g., Kushner et al., 2001; Marshall et al., 2006; Shindell & Schmidt, 2004), as well as the occurrence of extreme temperature and surface melt episodes in West Antarctica. For instance, Nicolas et al. (2017) found that the unusual extent and duration of the melting in the West Antarctica in January 2016 are linked to strong and sustained advection of warm marine air toward the area, likely favored by large-scale forcing (i.e., the concurrent strong El Niño event).

In addition to large-scale forcing, warm air masses can be episodically advected eastward over the orographic barrier of the AP, causing warm and dry downslope winds. This foehn event causes additional warming on the leeward side through different physical processes, such as latent release on the windward slopes

and isentropic drawdown (Brinkmann, 1971; Cape et al., 2015; Elvidge et al., 2016; Marshall et al., 2006; Oliva et al., 2017). Indeed, Cape et al. (2015) found that the frequency and duration of foehn events in the AP influenced regional temperature variability on hourly to seasonal time scales, suggesting that the increase in episodic foehn events was involved in the collapse of the Larsen B ice shelf during the austral summer season of 2001–2002. On the other hand, the extent to which the warming along the leeward side of the AP can be attributed to local-scale forcing (i.e., foehn effect warming), rather than to the large-scale advection of warm air from lower latitudes, is unknown. Although long-term temperature trends can be attributed to changes in circulation patterns that bring warmer air over the AP, local effects such as foehn wind have the potential to largely amplify the background large-scale warming, especially over the eastern part of the AP.

Here we document an extreme event of such warming amplification. On 24 March 2015, a maximum temperature of 17.5°C occurred at the Esperanza research base, located near the northern tip of the AP (see Figure 1). The event occurred just at the onset of the strong 2015–2016 El Niño event (between 18 and 27 March 2015), at the same time that the west coast of South America (northern, central, and southern Chile) was experiencing a series of extreme hydrometeorological events (Barrett et al., 2016; Bozkurt et al., 2016). Based on careful evaluation of several pieces of evidence (e.g., quality of observation, type and calibration of equipment, and foehn occurrence) by an international evaluation committee within the World Meteorological Organization Commission for Climatology, this extreme observation was certified as the highest temperature recorded for the Antarctic continent (Skansi et al., 2017).

The objective of this study is to describe the record high-temperature event in detail and to discuss how large-scale forcing played a key role in triggering the foehn event along the eastern part of the AP. We also aim to disentangle the role of large-scale forcing (i.e., warm air advection) versus local dynamics (i.e., foehn effect warming) by removing the surface topography in the northern part of the AP in a regional climate model (RCM) simulation. Section 2 provides a description of the data and methodology used in this study. Section 3 describes the observed local meteorological and synoptic conditions during the event based on surface station data, satellite imagery, and reanalysis data. Section 3 also includes a frequency analysis of dynamic and thermodynamic conditions of the event, based on 35 years of reanalysis data. Section 4 describes the modeling setup and shows the results from the control and topography removal simulations. The latter only differs from the control simulation in the surface topography conditions. Section 5 summarizes and discusses the results.

## 2. Data and Methods

### 2.1. Meteorological Stations

The spatial pattern of daily maximum temperature before and during the event (between 21 and 25 March 2015) over the AP was analyzed using the Global Historical Climatology Network data (Menne et al., 2012). The data are made available through the Chilean Climate Explorer's website (<http://explorador.cr2.cl>). Meteorological conditions at the windward and leeward sides of the northernmost tip of the AP were examined by using two surface stations: Carlini (formerly Jubany) and Esperanza, respectively. Data on 3-hourly near-surface air temperature (SAT), wind speed, and wind direction between 21 and 25 March 2015 for these two stations were obtained from the British Antarctic Survey server, which contains meteorological data available through the Scientific Committee for Antarctic Research. In order to put the daily maximum SATs in historical perspective for both the windward and leeward sides of the AP, we also calculated the frequency distribution of daily maximum SAT at Carlini and Esperanza stations for all days of March over the 1989–2015 and 1971–2015 periods, respectively. Data on surface precipitation at the Base San Martin station were also collected. The locations of meteorological stations used in this study, as well as the location of the radiosonde launching site at Rothera Research Station (used for model validation), are shown in Figure 1. Data on both surface and upper air are available at [ftp://ftp.bas.ac.uk/src/SCAR\\_EGOMA/](ftp://ftp.bas.ac.uk/src/SCAR_EGOMA/).

### 2.2. Satellite Imagery

Satellite imagery of the Larsen B Ice Shelf was obtained from the Moderate Resolution Imaging Spectroradiometer (MODIS) Antarctic Ice Shelf Image Archive (Scambos et al., 1996), provided by the National Snow and Ice Data Center (data available at [https://nsidc.org/data/iceshelves\\_images/](https://nsidc.org/data/iceshelves_images/)). We used two satellite images before and after the record high-temperature event (22 and 25 March 2015, respectively) in order to illustrate the impact of the foehn event and to thus evaluate short-term effects on the cryospheric processes.

To illustrate the large-scale cloudiness and water vapor conditions over the AP during the event, we obtained Antarctic composite infrared and water vapor imagery data for 24 March 2015 at 4 km spatial resolution, from the University of Wisconsin-Madison Antarctic Meteorological Research Center repository (data available at <ftp://amrc.ssec.wisc.edu/archive/2015/>).

### 2.3. Reanalysis Data

Atmospheric circulation during the event was analyzed using the European Centre for Medium-Range Weather Forecasts Reanalysis (ERA-Interim, hereafter ERAINT) data (Dee et al., 2011). Most reanalysis fields have a 6 h temporal resolution,  $0.75^\circ \times 0.75^\circ$  grid spacing, and 37 vertical levels. We used ERAINT daily mean sea level pressure, 500 hPa geopotential height ( $z_{500}$ ), and 850 hPa wind vectors in order to present the main synoptic conditions during the event. Regarding thermodynamics, daily vertically integrated water vapor (IWV) fields and integrated vapor transport (IVT) fields were calculated by using ERAINT daily mean meridional and horizontal winds and specific humidity ( $q$ ) from 1,000 to 300 hPa pressure levels:

$$IWV = \frac{1}{g} \int_{1,000}^{300} q dp \quad (1)$$

$$IVT = \sqrt{\left(\frac{1}{g} \int_{1,000}^{300} qu dp\right)^2 + \left(\frac{1}{g} \int_{1,000}^{300} qv dp\right)^2} \quad (2)$$

where  $g$  is the acceleration due to gravity ( $\text{m s}^{-2}$ ),  $q$  is specific humidity ( $\text{kg kg}^{-1}$ ),  $u$  and  $v$  are zonal and meridional winds ( $\text{m s}^{-1}$ ), respectively, and  $dp$  is the pressure difference between adjacent pressure levels.

We also used time series and frequency analysis of daily  $z_{500}$ , zonal wind speed at 850 hPa, air temperature at 850 hPa, and instantaneous vapor transport (VT) at 850 hPa during the 1980–2015 period in order to explore how unusual the thermodynamic and dynamic conditions were during the record high-temperature event. We performed this analysis only for late summer/early fall (January–February–March, JFM) months, as both large- and local-scale events can cause temperatures to rise above freezing, resulting in surface melting during these months (e.g., Nicolas et al., 2017).

Finally, we analyzed the daily maximum SAT anomaly on 24 March 2015 with respect to the long-term daily climatological mean (1979–2014). Based on the simulated data, we interpolated ERAINT daily maximum SAT anomalies to the model grid to better analyze grid-based warming on the lee side of the AP.

### 2.4. Blocking and Stability From Simulated Data

Numerical simulations (see section 4) were used to further investigate the moisture flux and orographic precipitation enhancement on the windward side and associated foehn warming on the leeward side. Dry and moist Froude numbers ( $Fr_d$  and  $Fr_m$ , respectively) were calculated in order to quantify the degree of blocking of the impinging airflow by the AP mountain range:

$$Fr_d = \frac{\bar{U}}{N_d H} \quad (3)$$

$$Fr_m = \frac{\bar{U}}{N_m H} \quad (4)$$

where  $\bar{U}$  is the mean-state layer-average (between 1,000 hPa and 850 hPa) wind speed ( $\text{m s}^{-1}$ ) and  $H$  is the characteristic mountain height ( $\sim 1,500$  m).  $N$  is the Brunt – Väisälä frequency (representing static stability). We calculated dry and unsaturated moist Brunt – Väisälä frequencies ( $N_d$  and  $N_m$ , respectively) as

$$N_d^2 = \frac{g}{\bar{\theta}} \frac{d\theta}{dz} \quad (5)$$

$$N_m^2 = \frac{g}{\bar{\theta}_v} \frac{d\theta_v}{dz} \quad (6)$$

where  $\bar{\theta}$  and  $\bar{\theta}_v$  are the mean-state layer-average (between 1,000 hPa and 850 hPa) potential temperature and virtual potential temperature, respectively. Following Kunz and Wassermann (2011), we combined  $Fr_d$  with

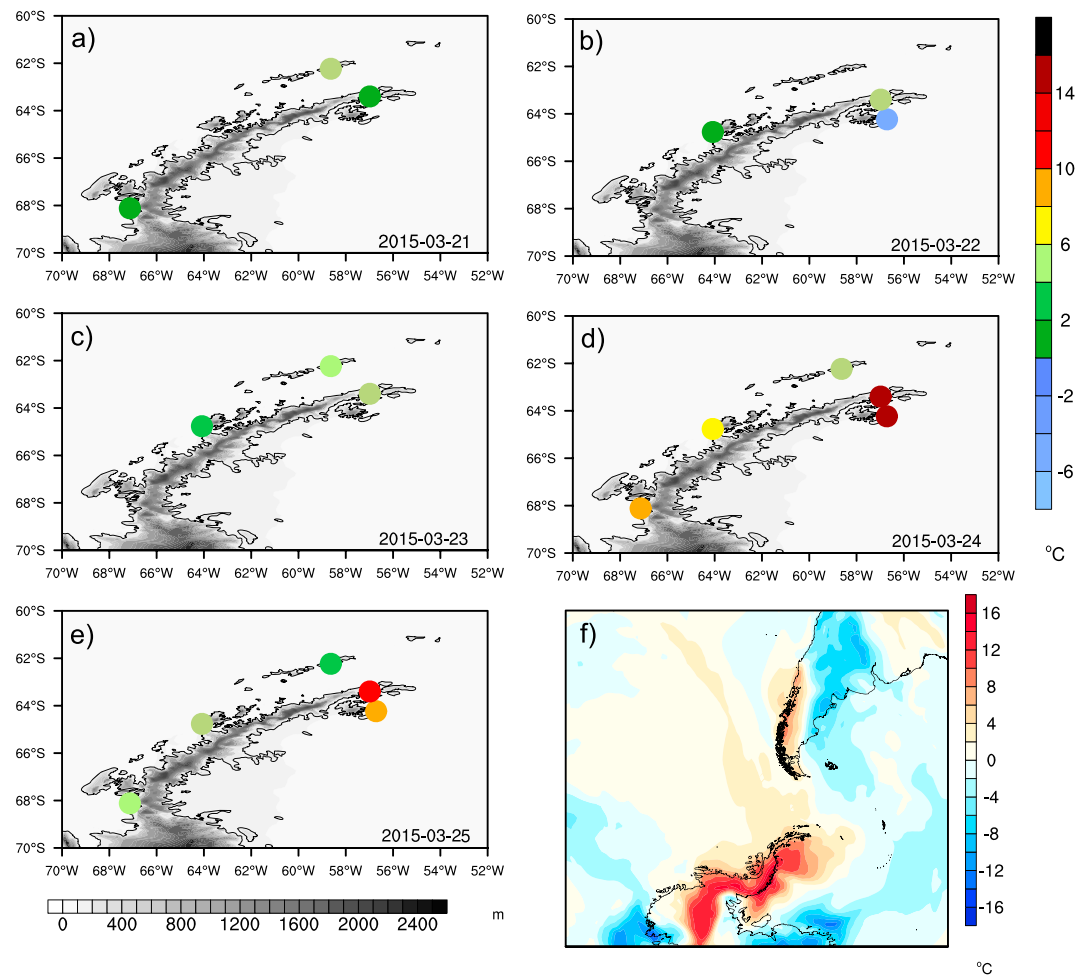


**Figure 2.** (a–e) Daily maximum near-surface air temperature distribution over the northern part of the AP between 21 and 25 March 2015. The background topography is derived from ETOPO2v2 at a horizontal grid spacing of 2 min (ETOPO2v2, 2006). (f) Spatial distribution of daily maximum temperature anomaly on 24 March 2015 with respect to the long-term daily maximum temperature climatological mean (24 March, 1979–2014) ERA-Interim reanalysis.

the local incoming moisture flux and related them to precipitation rates between higher elevations and lower elevations (i.e., shoreline) on the windward side:

$$\psi = \widehat{Fr}_d \cdot \widehat{F}_{WV} \tag{7}$$

where  $\psi$  is the potential precipitation parameter,  $\widehat{Fr}_d$  is the normalized dry Froude number, and  $\widehat{F}_{WV}$  is the normalized mean-state layer-average (between 1,000 hPa and 850 hPa) local incoming horizontal water vapor flux. Note that normalization is based on the maximum and minimum values (e.g.,  $(Fr_d - Fr_{dmin}) / (Fr_{dmax} - Fr_{dmin})$ ).  $\psi$  is a measure of potential orographic precipitation enhancement over the windward side, and it combines both the blocking by the topography and effect of the moisture flux. As noted by Kunz and Wassermann (2011), this parameter accounts for both the strength of the orographic lifting associated with the flow-over and flow-around regimes and the upper limit moisture that can be converted into precipitation.

### 3. Observation of the Event

#### 3.1. Local Conditions

Surface conditions of the record-breaking SAT event were investigated using the surface meteorological stations. Figures 2a–2e show the observed daily maximum SAT over the northern part of the AP between 21 and 25 March 2015. Overall, temperatures at the stations located on the windward side are cooler than those on the leeward side. However, on 21 March 2015, the SAT value at the Carlini station on the windward side (4°C) was greater than that at the Esperanza station on the leeward side (0°C) due to the large-scale warm air

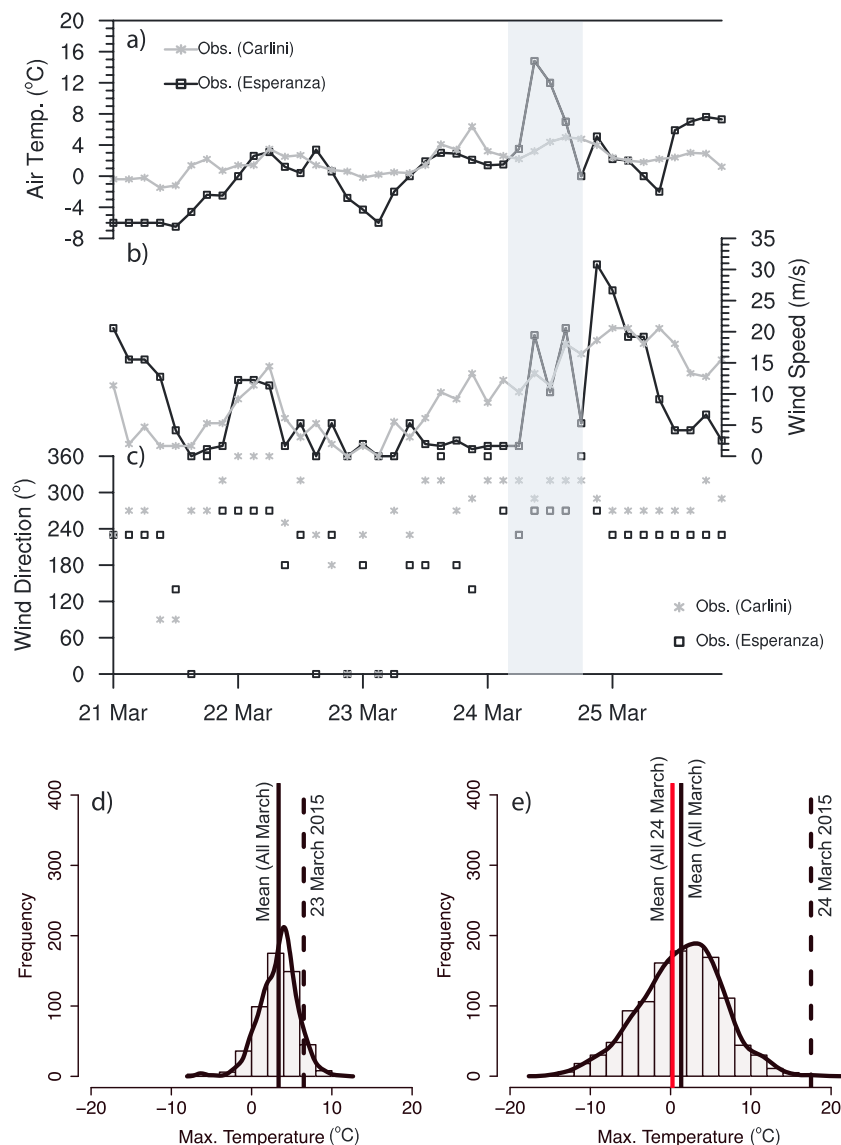


**Figure 3.** (a) Three-hourly near-surface air temperature, (b) wind speed, and (c) wind direction time series at the windward and leeward stations (Carlini and Esperanza, respectively) between 21 and 25 March 2015. Also shown is the frequency distribution of daily maximum near-surface air temperature for all days of March over the 1989–2015 and 1971–2015 periods for the Carlini (d) and Esperanza (e) stations, respectively. Light shading highlights the period when the foehn event occurred. Vertical solid black lines correspond to the mean value for all days of March at both stations. Vertical dashed black lines correspond to daily maximum near-surface air temperature on 23 and 24 March 2015, for Carlini and Esperanza, respectively. The vertical solid red line indicates the mean value for all days of 24 March. Solid lines in (d) and (e) are fitted distributions.

advection toward the windward areas (Figure 2a). On 24 March 2015, the higher temperatures were recorded at the Esperanza and Marambio stations (17.5°C and 17.4°C, respectively) on the leeward side of the northern tip of the AP (Figure 2d). On the same day, higher-temperature values also occurred also on the windward side of the AP. For instance, an all-time record temperature of 11.3°C was registered at the Base Arturo Prat station (between the period of 1985–2015). Another extreme SAT value was recorded at the Base San Martin station (10.5°C, the fourth highest March temperature for the 1980–2015 period). Extreme temperatures registered at meteorological stations on the windward side highlight the impact of the anomalous large-scale warm air advection on the AP.

The spatial distribution of the daily maximum temperature anomaly on 24 March 2015, calculated with respect to the long-term daily (24 March) climatological mean based on ERAINT (1979–2014), is shown in Figure 2f.

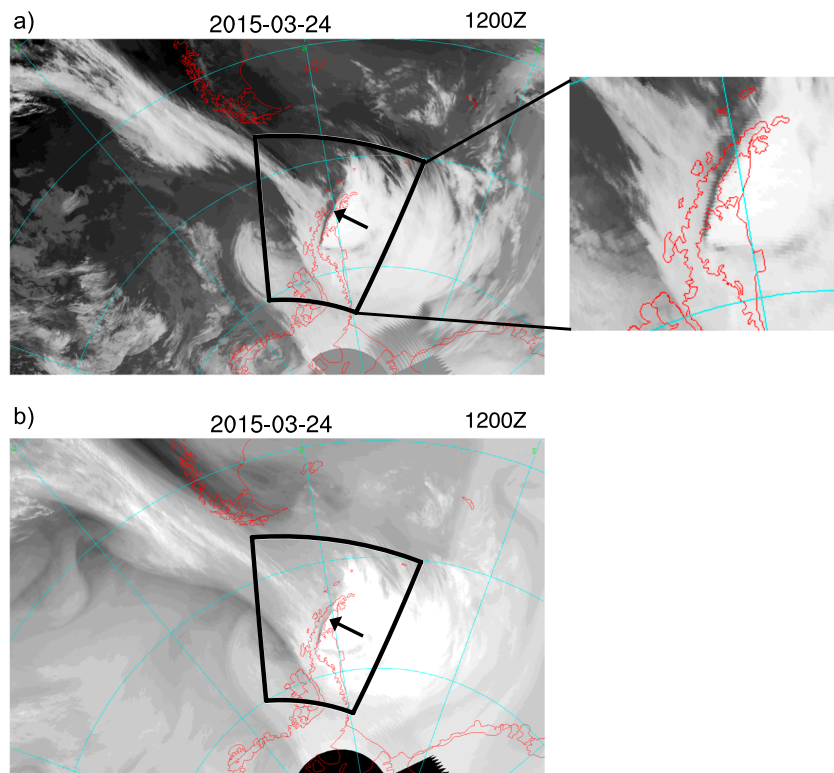


**Figure 4.** (a) The 24 March 2015 Antarctic composite infrared and (b) water vapor imagery data at 4 km spatial resolution. Arrow indicates the location of foehn-gap.

Positive temperature anomalies are not only confined to northern parts of the AP but also evident in the center and southern parts of the AP, with warm temperature anomalies ranging between +6 and +16°C.

Further investigation of windward and leeward meteorological conditions using 3 h data of SAT, wind speed, and wind direction between 21 and 25 March 2015 for the Carlini and Esperanza stations was performed (Figure 3). The characteristic signature of a foehn wind event is well illustrated at the Esperanza station (Figures 3a and 3b). For instance, the onset of the foehn event (24 March 2015, 0900 UTC) was marked by a rapid increase in wind speed (from  $1.5 \text{ m s}^{-1}$  to  $19.5 \text{ m s}^{-1}$ ) with a westerly/northwesterly direction, accompanied with an SAT  $> 10^\circ\text{C}$ . Just prior to the foehn onset, meteorological conditions at the Esperanza station were calm and stable, with the SAT ranging between 0 and  $4^\circ\text{C}$ . It is interesting to note that on 23 March, there was a slight increase in temperature at the Esperanza station (from  $-6$  to  $0^\circ\text{C}$ ) when the surface winds were around  $2\text{--}3 \text{ m s}^{-1}$ , which highlights the effect of large-scale advection of temperature and humidity before the foehn onset (see section 3.2). By comparison, the Carlini station shows only a very slight increase in SAT ( $3^\circ\text{C}$ ), with a maximum temperature ( $6.4^\circ\text{C}$  on 23 March 2015, 2100 UTC) occurring before the onset of the foehn event at the Esperanza station.

Figures 3d and 3e show the frequency distributions of long-term daily maximum SAT for all days of March for the Carlini (windward, 1989–2015 period) and Esperanza (leeward, 1971–2015 period) stations. The maximum SAT at the Carlini station ( $6.4^\circ\text{C}$ ) recorded on 23 March 2015 is close to the mean value ( $3.4^\circ\text{C}$ ), which hardly qualifies as an extreme case (Figure 3d). An intriguing question regarding the lack of extreme SAT anomalies at the Carlini station (despite the existence of the extremely moist and warm conditions on the windward side of the AP) remains. This may be related to diabatic cooling because of precipitation, as well as its location at the outer edge of the moisture advection (see section 3.2). On the other hand, a daily maximum SAT value ( $17.5^\circ\text{C}$ ) observed on 24 March 2015 at the Esperanza station stands out very clearly from the mean March value ( $1.3^\circ\text{C}$ , + $16.2^\circ\text{C}$  anomaly) observed between the 1971–2015 period, indicating the impact of foehn warming along the lee side. Note that the long-term mean daily maximum SAT value for 24 March is  $0.2^\circ\text{C}$  (vertical red line),  $17.3^\circ\text{C}$  below the maximum temperature recorded during the event.

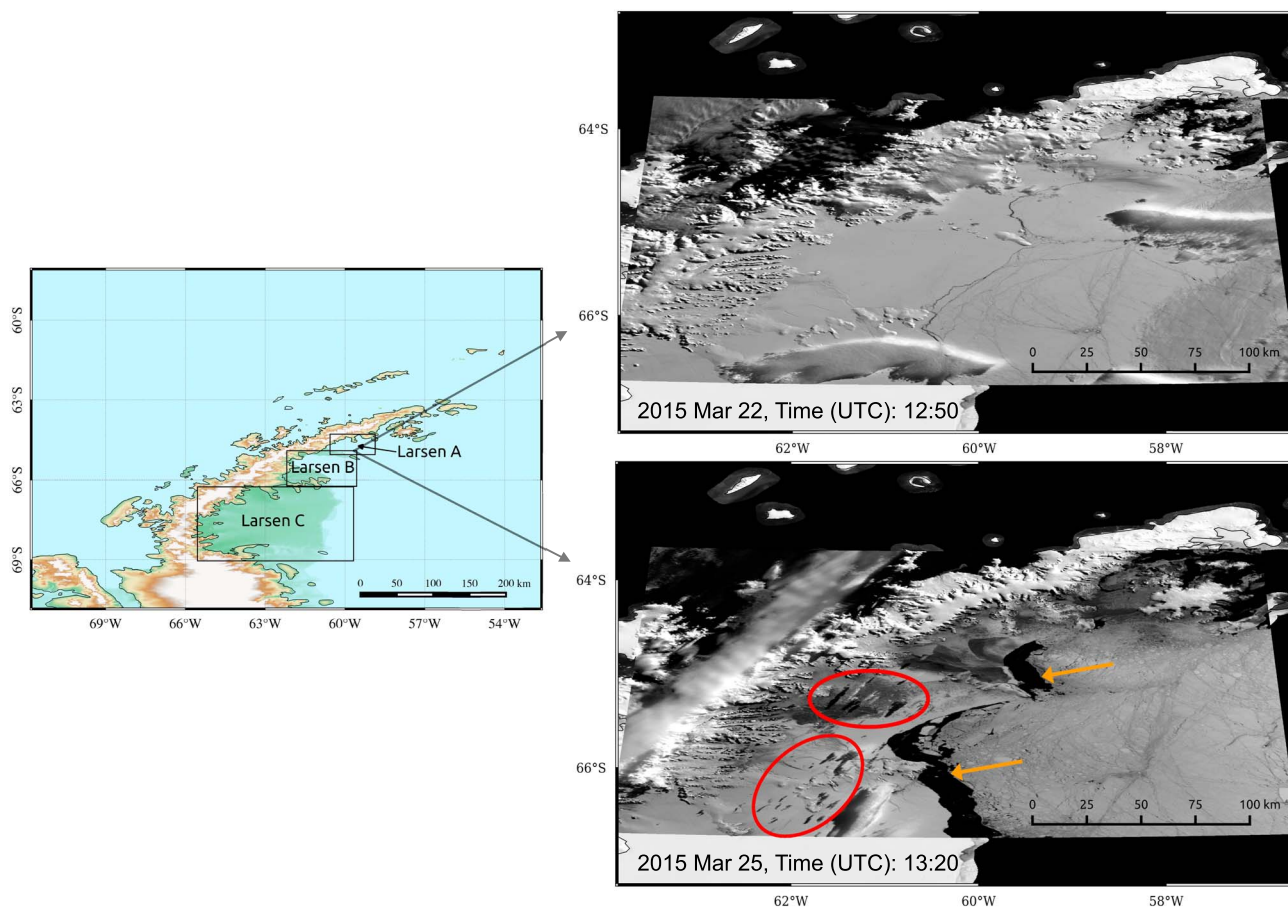


**Figure 5.** MODIS images of Larsen B and Larsen A embayments before (22 March 2015, 12:50 UTC) and after (25 March 2015, 13:20 UTC) the record high-temperature event. Orange arrows indicate areas of sea ice disintegration and offshore advection. Red circles contain dark patches on the fast ice and glacier surface (melt ponds).

Antarctic composite infrared imagery data for 24 March 2015 clearly shows the existence of a cloud-free zone or “foehn-gap” oriented north-south, just on the leeward side of the northern AP (Figure 4a). The infrared image shows that downstream clouds are brighter and colder than clouds upstream from the gap, indicating the formation of a patch of dense cirrus clouds. The foehn gap is also evident in the water vapor image which also confirms that water vapor is being transported from the midlatitudes (Figure 4b). Furthermore, from the images of the foehn-gap, one can deduce an approximate size of the descent of about 350 km in length, with a width of 20–60 km.

As noted before, glacier retreats and ice mass loss have occurred in recent years due to the rapid warming over the AP (e.g., Cook et al., 2005; Rignot et al., 2004; Scambos et al., 2004). Most recently, in July 2017, a massive iceberg calved away from the Larsen C Ice Shelf in the AP (Voosen, 2017). To trace the immediate impact of the foehn event and rapid temperature increase on the cryosphere, particularly on the leeward side of the northern AP, we examined two snapshots from the MODIS Antarctic Ice Shelf Image Archive over Larsen B and Larsen A, before and after the record high-temperature event (i.e., 22 and 25 March 2015, respectively). Figure 5 shows evidence of sea ice disintegration and melt pond formation on land-fast ice in the Larsen A and Larsen B embayments, consistent with the impact of foehn winds on the surface cryosphere (e.g., Ashmore et al., 2017; Elvidge et al., 2016). The satellite images clearly illustrate that a single, short-lived but extreme foehn warming can have a significant impact on the surface cryosphere by largely amplifying the warming signal produced by the large-scale warm advection.

### 3.2. Synoptic Conditions

The main synoptic-scale features during the extreme temperature event were a deep low-pressure center located over the Amundsen-Bellinghousen Sea, and a northwest-southeast oriented blocking ridge,



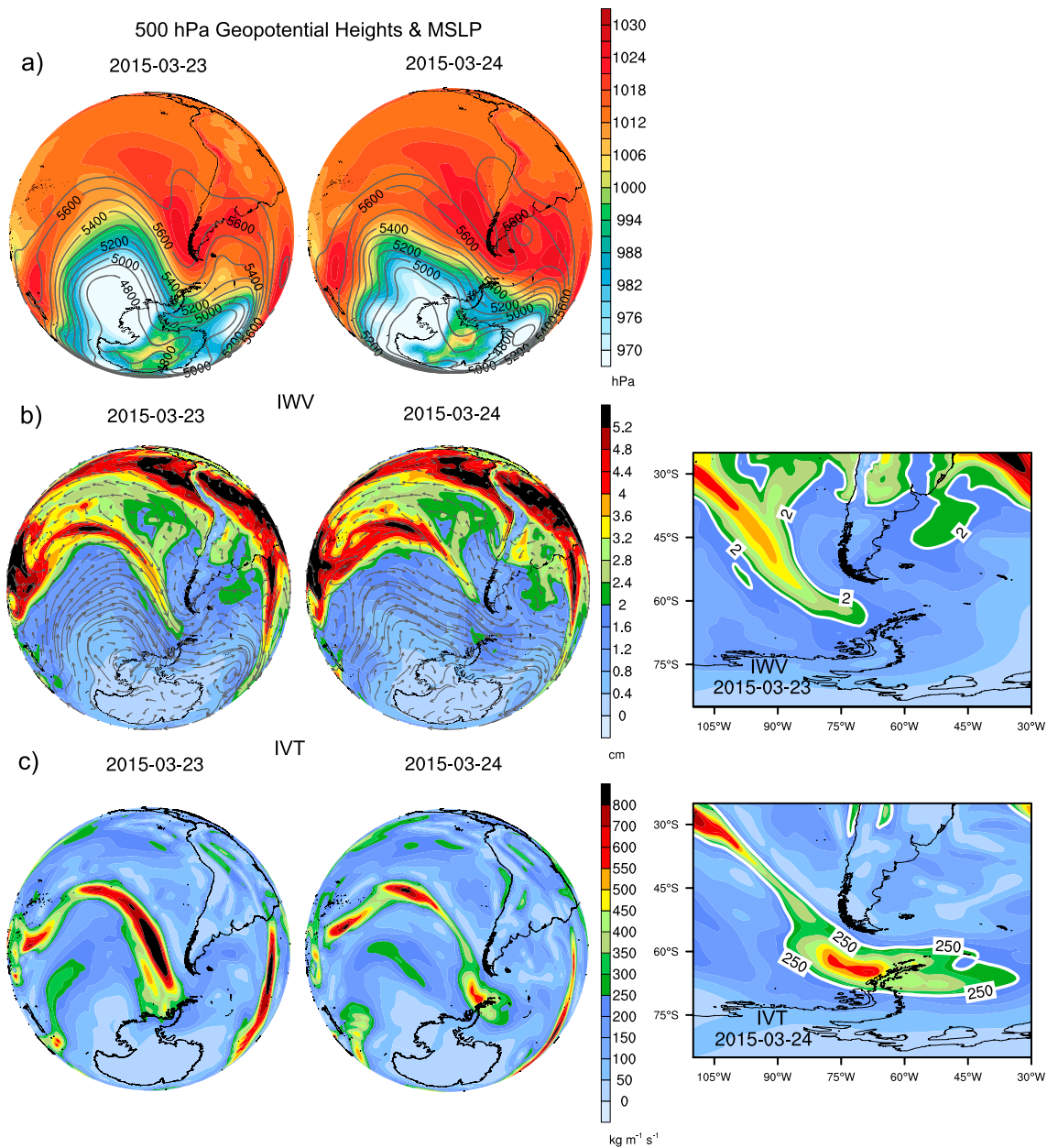


**Figure 6.** (a) The 23–24 March 2015 mean sea level pressure (hPa; shaded) and  $z_{500}$  (m; contour lines at 100 m intervals) from ERA-Interim (ERAINT). (b) The 23–24 March 2015 integrated water vapor (cm; shaded) and 850 hPa wind vectors from ERAINT. (c) The 23–24 March 2015 integrated vapor transport ( $\text{kg m}^{-1} \text{s}^{-1}$ ) from ERAINT. White contour lines in the zoom plots on the right correspond to integrated water vapor (IWV) and integrated vapor transport (IVT) thresholds (2 cm and  $250 \text{ kg m}^{-1} \text{s}^{-1}$ , respectively).

extending from the southeastern Pacific to the AP (Figure 6a). These synoptic conditions were favorable for inducing a large-scale warm air advection from subtropical latitudes to the AP. Such blocking situations assure meridional heat and moisture flux toward the Antarctic coast (e.g., Schlosser et al., 2014; Uotila et al., 2013). A 96 h backward trajectory analysis based on the Global Data Assimilation System on  $0.50 \times 0.50^\circ$  grids confirms that the air masses that arrived to the Esperanza station on 23 March 2015 at 21:00 UTC, originated over the subtropical Pacific Ocean (near to  $35^\circ\text{S}$ ,  $110^\circ\text{W}$ ) on 20 March 2015 at 00:00 UTC (Figure S1 in the supporting information).

The large-scale circulation pattern steered an intense northwest-southeast atmospheric river (AR) (Figures 6b and 6c), which reached the AP on 23 March 2015. Several studies define ARs as midlatitude areas, with an IWV

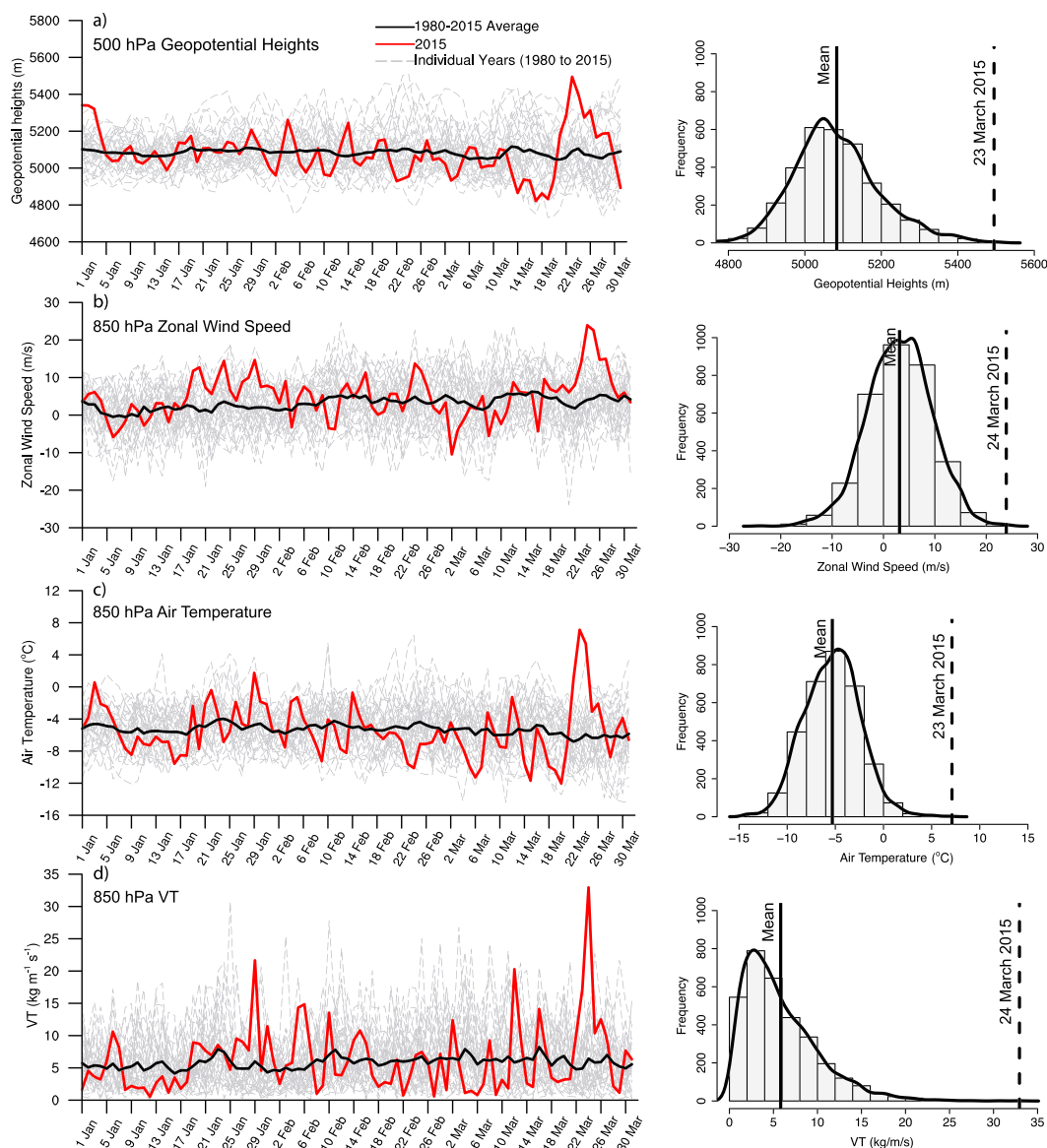


**Figure 7.** Long-term (1980–2015, gray dashed lines) January–February–March daily time series of (a)  $z_{500}$  (m), (b) zonal wind speed ( $\text{m s}^{-1}$ ), (c) air temperature ( $^{\circ}\text{C}$ ), and (d) vapor transport (VT) ( $\text{kg m}^{-1} \text{s}^{-1}$ ) at 850 hPa for a grid point on the windward side of the AP. The solid lines indicate the 1980–2015 (black) and 2015 (red) mean fields. Also shown are ERA-Interim daily frequency distribution of each of the aforementioned variables for January–February–March between 1980 and 2015. The vertical solid line corresponds to the long-term mean, and the vertical dashed lines correspond to the value and date of the extreme event.

greater than 2 cm, narrower than 1,000 km, and longer than approximately 2,000 km (e.g., Dettinger et al., 2011; Gimeno et al., 2014; Ralph et al., 2004; Viale & Nuñez, 2011). According to the Glossary of Meteorology (American Meteorological Society, 2017), lateral boundaries in ARs can be defined based on the IVT threshold of  $250 \text{ kg m}^{-1} \text{ s}^{-1}$ . Figure 6b shows a long, narrow corridor of IWV ( $> 2 \text{ cm}$ ) that approaches the northern part of the AP on 23 March, satisfying the AR definition. Yet IWV values decrease below 2 cm along the coastal zone of the AP. Nevertheless, given the fact that the capacity of the atmosphere to hold moisture is reduced in polar regions, Gorodetskaya et al. (2014) identified the ARs using an IWV percentile-based threshold by taking into consideration the decreased saturation capacity of the polar troposphere; they stated that the IWV can drop below the commonly used threshold of 2 cm near the Antarctic coast. Larger IVT values ( $> 250 \text{ kg m}^{-1} \text{ s}^{-1}$ ) over the northern AP on 24 March also confirm and satisfy the AR conditions during 23–24 March.

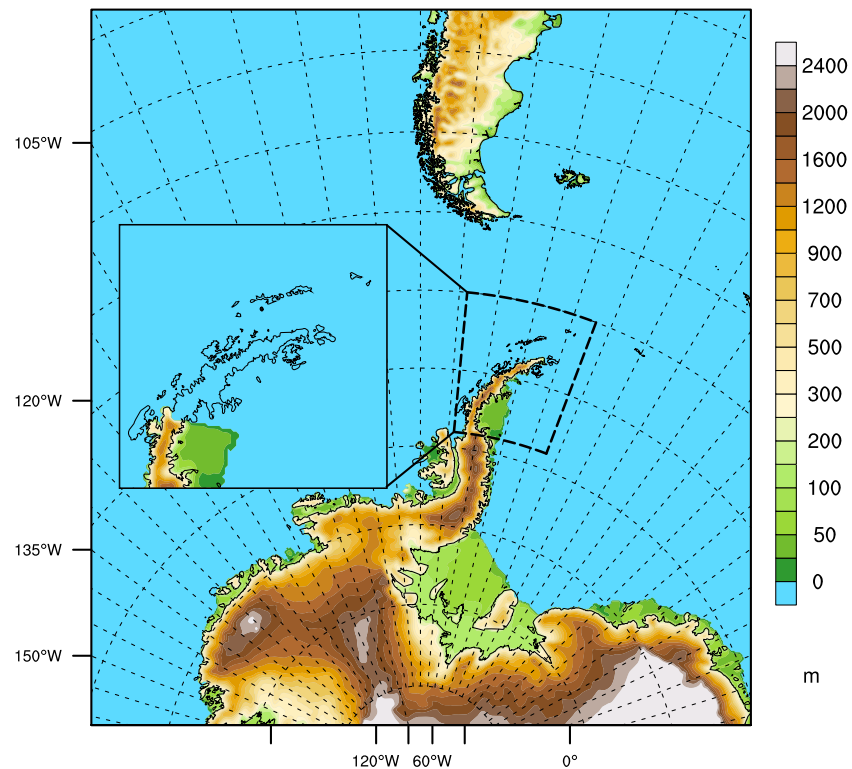


**Figure 8.** Topography (m) in the model domain at 10 km resolution. The zoom plot shows the region where the topography is completely removed in the sensitivity simulation. Note that the model still includes ice-covered land in the NOTOPO experiment.

Finally, we explore whether the dynamic and thermodynamic conditions during the extreme temperature event were unusual with respect to climatological conditions from ERA-Interim (1980–2015). The left column in Figure 7 shows the long-term (1980–2015) JFM daily time series of  $z_{500}$  (m) and zonal wind speed at 850 hPa ( $u_{850}$ ,  $\text{m s}^{-1}$ ), air temperature at 850 hPa ( $T_{850}$ ,  $^{\circ}\text{C}$ ), and VT at 850 hPa ( $VT_{850}$ ,  $\text{kg m}^{-1} \text{s}^{-1}$ ) for a grid point located in the upstream region of the AP ( $\sim 150$  km far from the AP;  $64.5^{\circ}\text{S}$ ,  $66^{\circ}\text{W}$ ). The time evolution of  $z_{500}$  indicates an anomalous sudden increase starting from 19 March and reaching a maximum on 23 March 2015, with a departure of  $\sim 420$  m, just 1 day before the event. Accordingly,  $u_{850}$  reaches the highest value ( $\sim 24 \text{ m s}^{-1}$ ) on 24 March 2015 with a departure of  $\sim 20 \text{ m s}^{-1}$  from the mean field. The frequency distributions of  $z_{500}$  and  $u_{850}$  reveal that the upper-level and low-level dynamic conditions were extremely anomalous before and during the event (e.g.,  $\sim 5,495$  m on 23 March 2015 and  $24 \text{ m s}^{-1}$  on 24 March 2015) but do not represent the most extreme cases (i.e.,  $z_{500}$  was the third highest, and  $u_{850}$  was the second highest of all JFM records between 1980 and 2015).

In terms of thermodynamic conditions, Figure 7c indicates the existence of an anomalous, low-level air temperature warming during the event. Starting from 20 March 2015,  $T_{850}$  values indicate a rapid increase, reaching a maximum value of  $7.1^{\circ}\text{C}$  on 23 March 2015 (an  $\sim 12^{\circ}\text{C}$  departure from the mean field). In accordance with high IWV values (see Figure 6b), the  $VT_{850}$  between 21 and 24 March 2015 also reveals a very sharp increase, with a maximum value of  $32.9 \text{ kg m}^{-1} \text{s}^{-1}$  occurring on 24 March 2015 (a  $27 \text{ kg m}^{-1} \text{s}^{-1}$  departure from the mean field, Figure 7d). Frequency distributions of thermodynamic conditions indicate the most extreme conditions (more pronounced in  $VT_{850}$  values) standing out very clearly from the mean values observed in the reanalysis during late summer/early fall in the last 35 years.

#### 4. Numerical Simulations

The steep terrain and harsh climate of the eastern AP have historically prevented the deployment of an extensive observational network and have complicated the maintenance of available meteorological stations (van Wessem et al., 2015). This has imposed a limitation on the data that can be used in diagnostic

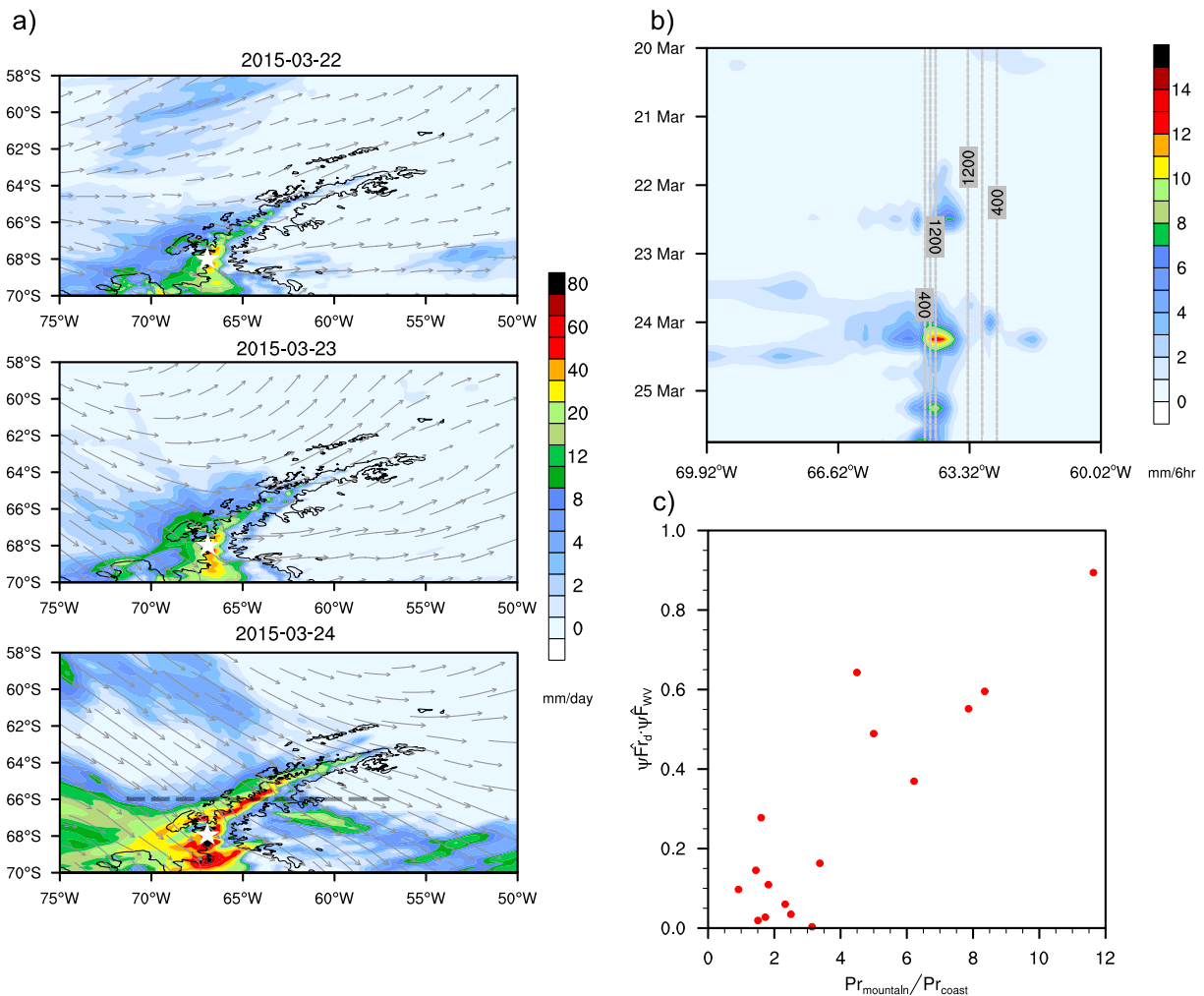


**Figure 9.** (a) Simulated precipitation ( $\text{mm d}^{-1}$ ) and 850 hPa wind vectors ( $\text{m s}^{-1}$ ) from RegCM4 at 10 km spatial resolution between 22 and 24 March 2015. The horizontal dashed line indicates the cross-section line, and white stars show the location of Base San Martin. (b) The time-longitude (Hovmöller) diagram of 6 h precipitation rates at 66°S shown by the dashed line in Figure 9a. Vertical dashed gray lines indicate elevation values at the corresponding longitude points. (c) Ratio of precipitation in the mountains to precipitation at the shoreline along 66°S as a function of the precipitation parameter,  $\psi$ , which is the product of normalized dry Froude number ( $\hat{F}_{r_d}$ ) and normalized mean-state layer-average (between 1,000 hPa and 850 hPa) local incoming horizontal water vapor flux ( $\hat{F}_{WV}$ ) between 20 and 25 March 2015.

and case studies. One common method of overcoming the difficulties arising from the inadequate observational network is to use RCMs to represent the main climatic features at high spatial resolutions ( $\leq 10$  km). A number of regional weather and climate model simulations have been employed over the Antarctic continent to gain a detailed description of climate conditions, as well as to understand the physical mechanisms operating during foehn wind events (e.g., Elvidge et al., 2015; Speirs et al., 2013; van Wessem et al., 2014, 2015).

In this part of our study, we further investigate the foehn warming event over the AP by performing RCM experiments. The main purpose of this modeling experiment is to disentangle the role of the large-scale warm air advection versus the local topographically induced warming (i.e., foehn effect warming) through a topography removal experiment.

#### 4.1. Model Description and Experiment Design

We conducted a numerical experiment using RegCM4, a three-dimensional, primitive equation, hydrostatic RCM maintained by the International Centre for Theoretical Physics. RegCM4 is the latest version of the modeling system originally developed by Giorgi, Marinucci, and Bates (1993); Giorgi, Marinucci, Bates, and DeCanio (1993); and Pal et al. (2007). Its dynamical core is based on the hydrostatic version of the Penn State/National Center for Atmospheric Research mesoscale model MM5 (Grell et al., 1994). RegCM has been used in

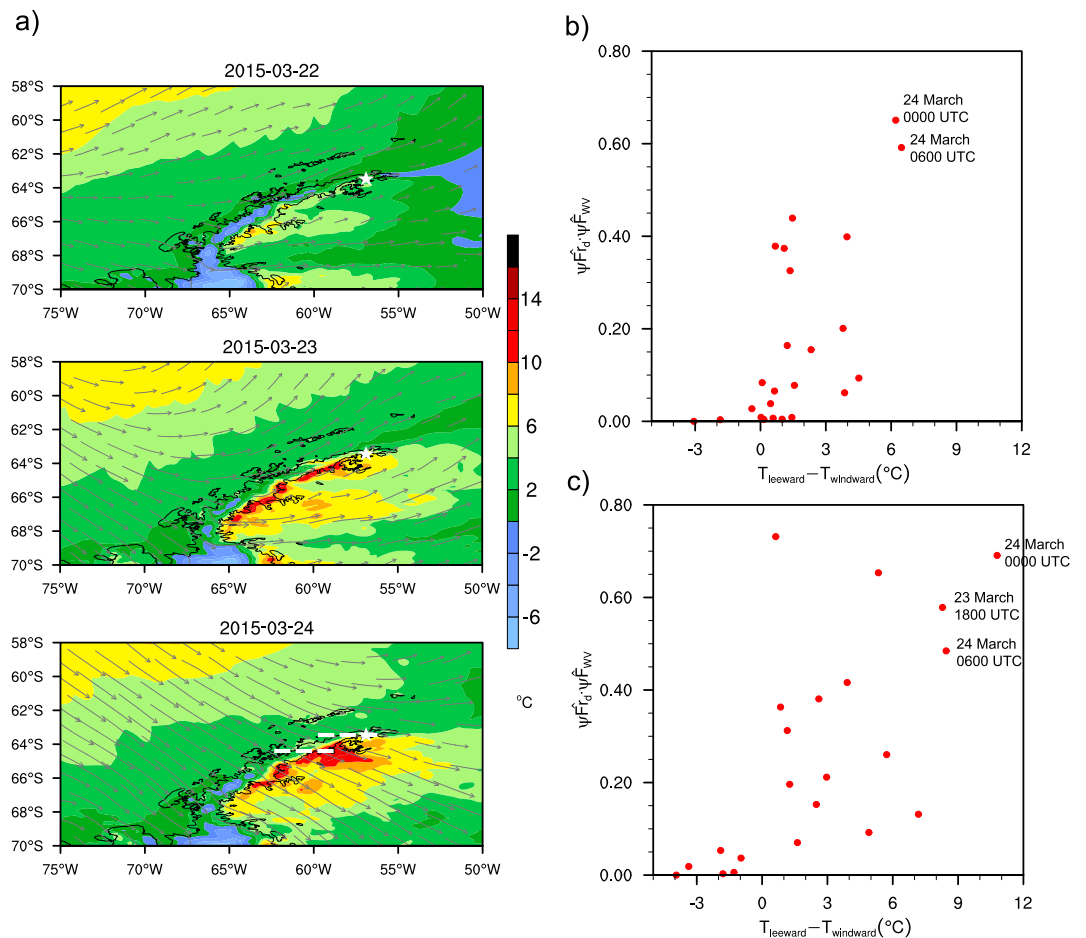


**Figure 10.** (a) Spatial distribution of daily maximum near-surface air temperature ( $^{\circ}\text{C}$ ) and 850 hPa wind vectors over the northern part of the peninsula between 22 and 24 March 2015 in CTR. Horizontal dashed lines indicate the cross-section line, and white stars show the location of the Esperanza station. (b, c) Scatter diagrams of near-surface air temperature differences ( $^{\circ}\text{C}$ ) between the leeward and windward sides of the AP as a function of the precipitation parameter ( $\psi$ , see section 2.4) along two lines over the northern tip and central part of the AP, respectively, between 20 and 25 March.

numerous RCM simulations, even over regions dominated by complex terrain features such as the Atacama Desert (Bozkurt et al., 2016), the Arctic and Mediterranean regions (Grassi et al., 2013), and European Alps (Giorgi et al., 2016). The physical schemes (e.g., Anthes, 1977; Dickinson et al., 1993; Emanuel, 1991; Grell, 1993; Holtslag et al., 1990; Kiehl et al., 1996; Pal et al., 2000; Zeng et al., 1998) used within the model are described in the supporting information (Text S1). A more detailed description of the model and physical parameterizations can be found in Giorgi et al. (2012).

The modeling experiment consists of a 17 day simulation (15–31 March 2015), for which RegCM4 was run with initial and boundary conditions provided by the ERAINT available at 6 h intervals, with a grid spacing of  $0.75^{\circ} \times 0.75^{\circ}$ . Twelve grid points in each direction were allocated for each lateral buffer zone in which the model prognostic variables were nudged to the boundary conditions with an exponential nudging coefficient proposed by Giorgi, Marinucci, Bates, and DeCanio (1993). The other input files used for boundary conditions (e.g., Reynolds et al., 2002) are described in the supporting information (Text S1). The simulations were performed on a domain at 10 km spatial resolution ( $512 \times 472$  grid cells) and 23 vertical levels using a Rotated Mercator projection (Figure 8). The modeling experiment includes a control simulation (hereafter CTR) that uses the default topographic features and a topography removal simulation (hereafter NOTOPO) that removes the surface topography of the northern part of the AP (Figure 8). Thus, the results of the NOTOPO simulation can be used to disentangle the role of the large-scale warm air advection versus the local topographically induced warming.

A model evaluation based on synoptic fields, surface meteorological conditions, and available sounding observation at the Rothera station is provided in full detail in the supporting information (Text S2 and Figures S2–S6). Overall, the model realistically reproduces the main synoptic fields and extreme dynamical and thermodynamical conditions before and during the event (Figures S2–S5). Despite the reasonable agreement in large-scale forcing and close estimation of the observed SAT time evolution, the model has difficulties in reproducing the steep SAT increase during the foehn onset (Figure S6). Given the fact that the AP hosts complex topographic features that are difficult to represent even in high-resolution dynamical downscaling experiments, we also performed a nonhydrostatic simulation with a relatively higher horizontal resolution (6 and 2 km) using the Weather and Research Forecast (WRF) model (Skamarock et al., 2008) in order to explore the impact of model resolution on simulated meteorological conditions. The physical schemes used in the WRF simulations (e.g., Hong & Lim, 2006; Main, 2004; Mlawer et al., 1997; Nakanishi & Niino, 2006), as well as the domain, are given in the supporting information (Text S3 and Figure S7). Results show that higher-resolution simulations also present difficulties in reproducing the observed near-surface conditions at specific point locations, particularly the steep SAT increase at foehn onset (see Figure S8). Previous RCM experiments over the AP have shown similar issues in reproducing near-surface conditions (e.g., Speirs et al., 2010). Despite the lack of agreement at the station level, both models reproduce a similar spatial pattern of SAT and foehn warming along the eastern part of the AP (Figure S9).

#### 4.2. Orographic Precipitation Enhancement and Foehn Characteristics in CTR Experiment

The anomalous water vapor reaching the windward side of the AP between 22 and 24 March resulted in accumulated precipitation values exceeding 50 mm at the Base San Martin station (a larger value than the long-term March average for that station). Between these dates, ERA-Interim also shows substantial precipitation on the windward side of the AP, particularly on 24 March (see Figure S10a). The model shows a similar spatial pattern of precipitation and reproduces the orographic precipitation on the windward side of the AP (Figure 9a). For instance, a large amount of precipitation is simulated on 24 March ( $>30 \text{ mm d}^{-1}$ , close to the observed value at the Base San Martin station) on the windward side of the AP (south of  $65^\circ\text{S}$ ).

A time-longitude (Hovmöller) diagram of 6 h precipitation rates at  $66^\circ\text{S}$  illustrates that maximum precipitation rates ( $>10 \text{ mm h}^{-1}$ ) are concentrated at high elevations between 400 m and 1,200 m on 24 March (Figure 9b). Figure 9c shows the ratio of precipitation in the mountains to that at the shoreline along  $66^\circ\text{S}$  as a function of  $\psi$  (the product of  $\widehat{Fr}_d$  and  $\widehat{F}_{WV}$  (see section 2.4)) between 20 and 25 March 2015. Despite the considerable scatter, a higher precipitation ratio between the mountain top and the shoreline tends to occur at high values of  $\psi$  (e.g., a ratio of 12 when  $\psi$  is  $\sim 0.9$ ), indicating the orographic enhancement of precipitation due to both an anomalous moisture flux and vertical stability change. Airflow at a chosen grid point along  $66^\circ\text{S}$  (close to the maximum precipitation) is characterized by low  $Fr_m$  (i.e.,  $Fr_m < 0.6$ , not shown) until 23 March 00 UTC, indicating an upstream blocking, and thus the associated precipitation fall upwind of the barrier (see Figure 9a, 22 and 23 March). Nevertheless, starting from 23 March, the  $Fr_m$  increases to values close to 1 (between 0.8 and 1.0, not shown) and, for instance, when the  $Fr_m$  is  $\sim 1.0$  on 24 March 06 UTC, the heaviest precipitation ( $>10 \text{ mm}$ ) falls along the barrier. Slightly larger  $Fr_m$  values ( $Fr_m > 1.0$ , not shown) on 24 March indicate that the flow tends to pass over the barrier, and some precipitation falls on the lee side (see Figure 9a, 24 March and the Hovmöller diagram).

Figure 10a shows the spatial distribution of daily maximum SAT and 850 hPa wind vectors between 22 and 24 March from the CTR experiment. Warm air advection from lower latitudes toward the windward side of the AP is clearly seen in the CTR simulation (Figure 10a). On 23 March, the AP is exposed to westerly and northwesterly flow, and topographically induced warming takes place on the leeward side of the AP mountain range. As shown in Figures 6, and 7a and 7c, the large-scale forcing (i.e., the tongue of warm, moist air reaching the AP) was more intense on 23 March. However, the maximum SAT at Esperanza took place 1 day later, on 24 March, because of a full-fledged development of the foehn event on that day.

Figures 10b and 10c also show the near-SAT difference between leeward and windward sides of the AP as a function of the precipitation parameter ( $\psi$ ) along two lines over the northern tip and central part of the AP, respectively, between 20 and 25 March. Despite the considerable scatter, there is a general tendency for temperature differences to increase (largest differences at foehn onset) as  $\psi$  increases at both the northern tip of the AP and in the central AP (with a more pronounced tendency). This indicates the contribution of latent heat release due to the orographic precipitation enhancement on the windward side, to the foehn warming on the leeward side. These results confirm that the model accurately captures the timing of foehn conditions

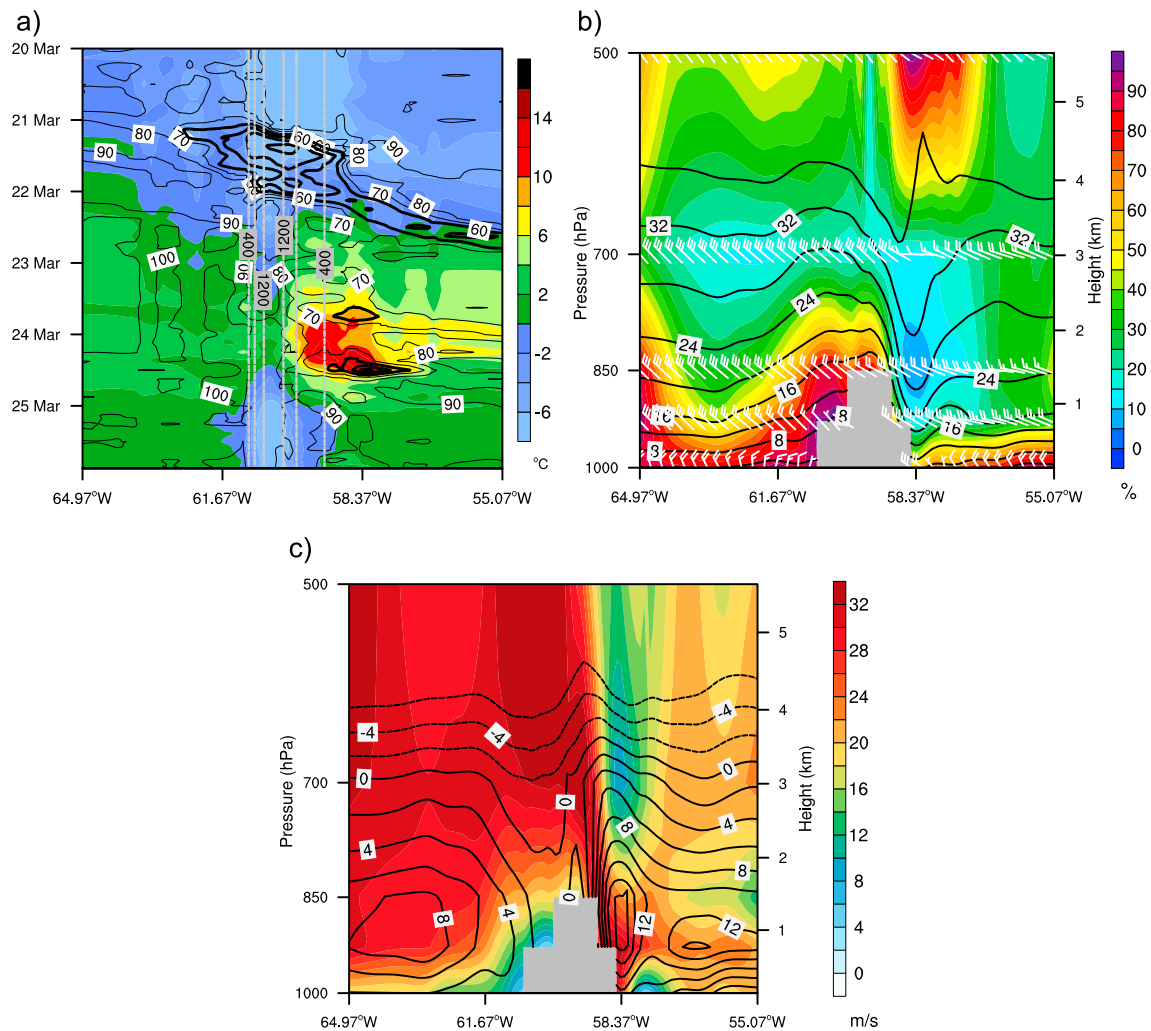


**Figure 11.** (a) Time-longitude diagram of 3 h near-surface air temperature ( $^{\circ}\text{C}$ ; shaded) and relative humidity (%; contour lines at 10% intervals) fields around  $64^{\circ}\text{S}$ , between 20 and 25 March 2015, from CTR experiment. Bold contour lines correspond to relative humidity values less than 60%. Vertical dashed gray lines indicate elevation values at the corresponding longitude points. (b) Vertical cross section of relative humidity (%; shaded), potential temperature ( $^{\circ}\text{C}$ ; contour lines at  $4^{\circ}\text{C}$  intervals), and wind barbs (white) around  $64^{\circ}\text{S}$  from the CTR experiment on 24 March 1200 UTC. (c) Same as (b) but for wind speed ( $\text{m s}^{-1}$ ; shaded) and air temperature ( $^{\circ}\text{C}$ ; contour lines at  $2^{\circ}\text{C}$  intervals). Note that gray shading corresponds to masked flux data when they fall beneath the surface pressure.

on 24 March, yet, compared to those at its northern tip, larger temperature differences between leeward and windward sides occur in the central parts of the AP. This is consistent with the findings of Elvidge et al. (2016), who revealed that a linear flow regime, characterized by stronger cross-peninsula winds over the central AP, where the higher mountain peaks are located, causes more extensive leeside warming and higher melting rates. Indeed, a slight change in the low-level wind field impinging the AP, from moderate westerlies on 23 March to stronger northwesterly winds (almost perpendicular to the AP mountain range) on 24 March, results in a marked warming ( $> 10^{\circ}\text{C}$ ) on the leeward side of the central AP.

A time-longitude (Hovmöller) diagram around  $64^{\circ}\text{S}$  (across the core of the largest SAT, see Figure 10a) of 3 h SAT and relative humidity ( $r$ ) fields between 20 and 25 March from the CTR simulation is shown in Figure 11a. A marked contrast in  $r$  takes place after 22 March, with very humid conditions ( $r \sim 100\%$ ) on the windward side and dry conditions ( $r < 60\%$ ) on the leeward side. Accordingly, remarkable warming is evident, particularly on 24 March at 1200 UTC, with an SAT exceeding  $12^{\circ}\text{C}$  on the leeward side. A vertical cross-section analysis of  $r$ , potential temperature ( $\theta$ ), and wind vectors from CTR at the time of the largest SAT occurrence on the leeward side (24 March 1200 UTC) illustrates a low-level blocking upstream and mountain wave activity, with warm and dry air aloft being advected downward to the surface on the leeward side. This feature also indicates the existence of an isentropic drawdown of warm air (e.g.,  $\theta \sim 28^{\circ}\text{C}$  and  $r \sim 10\%$  at 850 hPa) (Figure 11b).

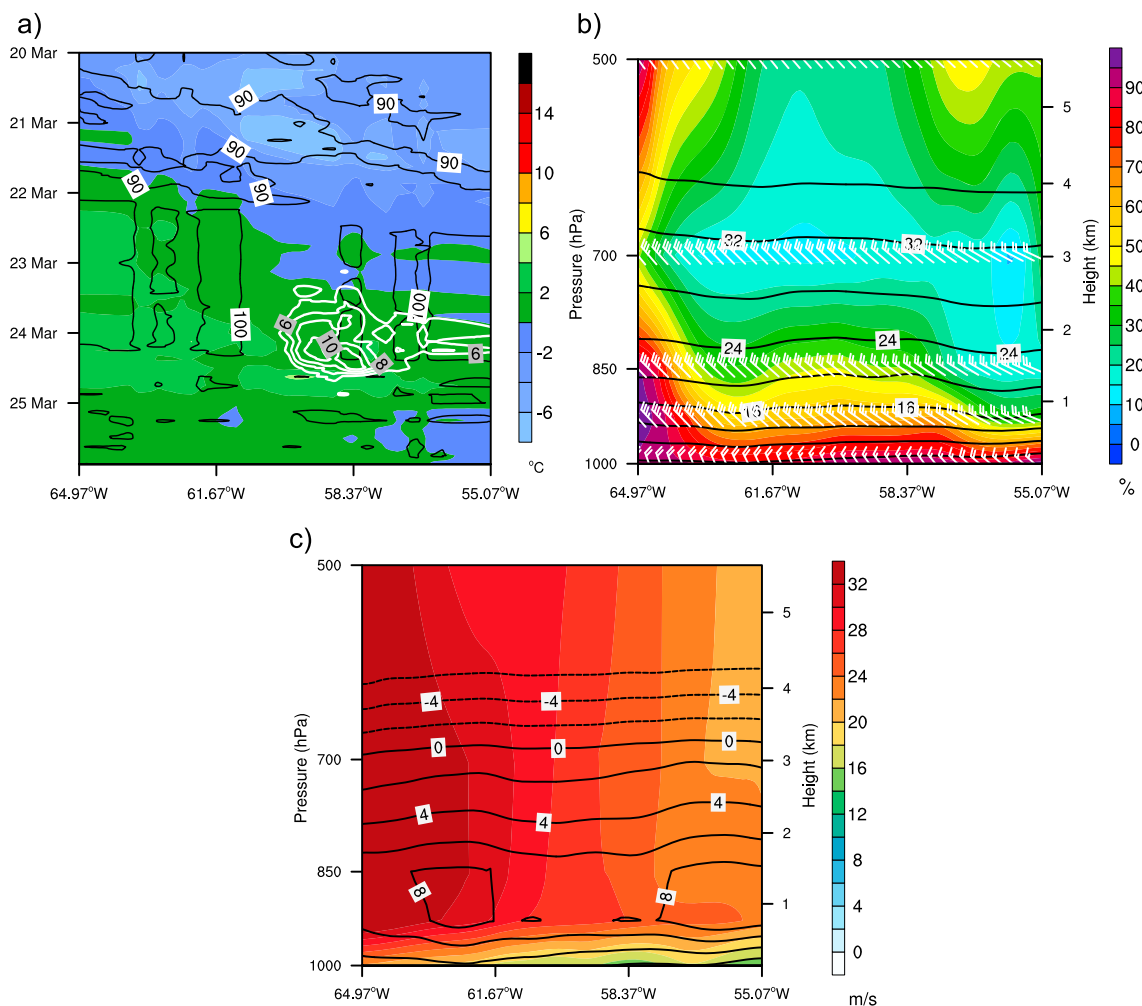


**Figure 12.** (a) Time-longitude diagram of 3 h near-surface air temperature (°C; shaded) and relative humidity (%; contour lines at 10% intervals) fields around 64°S, between 20 and 25 March 2015, from the NOTOPO experiment. White contour lines highlight the warming areas apparent in Figure 11a for the CTR experiment. (b) Vertical cross section of relative humidity (%; shaded), potential temperature (°C; contour lines at 4°C intervals), and wind barbs (white) around 64°S from the NOTOPO experiment on 24 March 1200 UTC. (d) Same as (c) but for wind speed ( $\text{m s}^{-1}$ ; shaded) and air temperature (°C; contour lines at 2°C intervals).

Very humid conditions ( $r > 90\%$ ) with calm wind speeds are evident on the windward side at the same time. The major upstream extent of the barrier winds was determined by a Rossby radius of deformation (see Text S4) and found to be about 135 km (typically around 150 km for the AP (Elvidge & Renfrew, 2016)). The width of dry air aloft ( $\sim 50$  km) in the model simulation is consistent with the foehn gap, as seen in the infrared image (Figure 4a). Elevated near-surface wind velocities ( $\sim 30 \text{ m s}^{-1}$ ) with marked warm air temperatures ( $> 12^\circ\text{C}$ ) along the lee slope highlight the impact of foehn-induced warming (Figure 11c). Similar fingerprints of the foehn effect exist over the northern tip of the AP ( $\sim 63.5^\circ\text{S}$ ), albeit with a less pronounced effect compared to that along the eastern part of the central AP (see Figure S11).

### 4.3. NOTOPO Experiment

The topographic removal in the NOTOPO experiment results in the disappearance of warming areas (shown with white contours), which clearly illustrates the impact of the surface topography on induced warming during the event (Figure 12a). The NOTOPO experiment reduces much of the warming ( $\sim 10^\circ\text{C}$ ) on the leeward side over the area where the core of the larger SATs ( $\sim 12^\circ\text{C}$ ) are observed in the CTR simulation. Removal of topography in the NOTOPO experiment prevents the subsidence of warm, dry air and mountain wave activity over the northern AP (Figure 12b). Elevated near-surface wind velocities with marked warm air temperatures along the lee slope in the CTR simulation (see Figure 11c) dramatically disappear in the NOTOPO



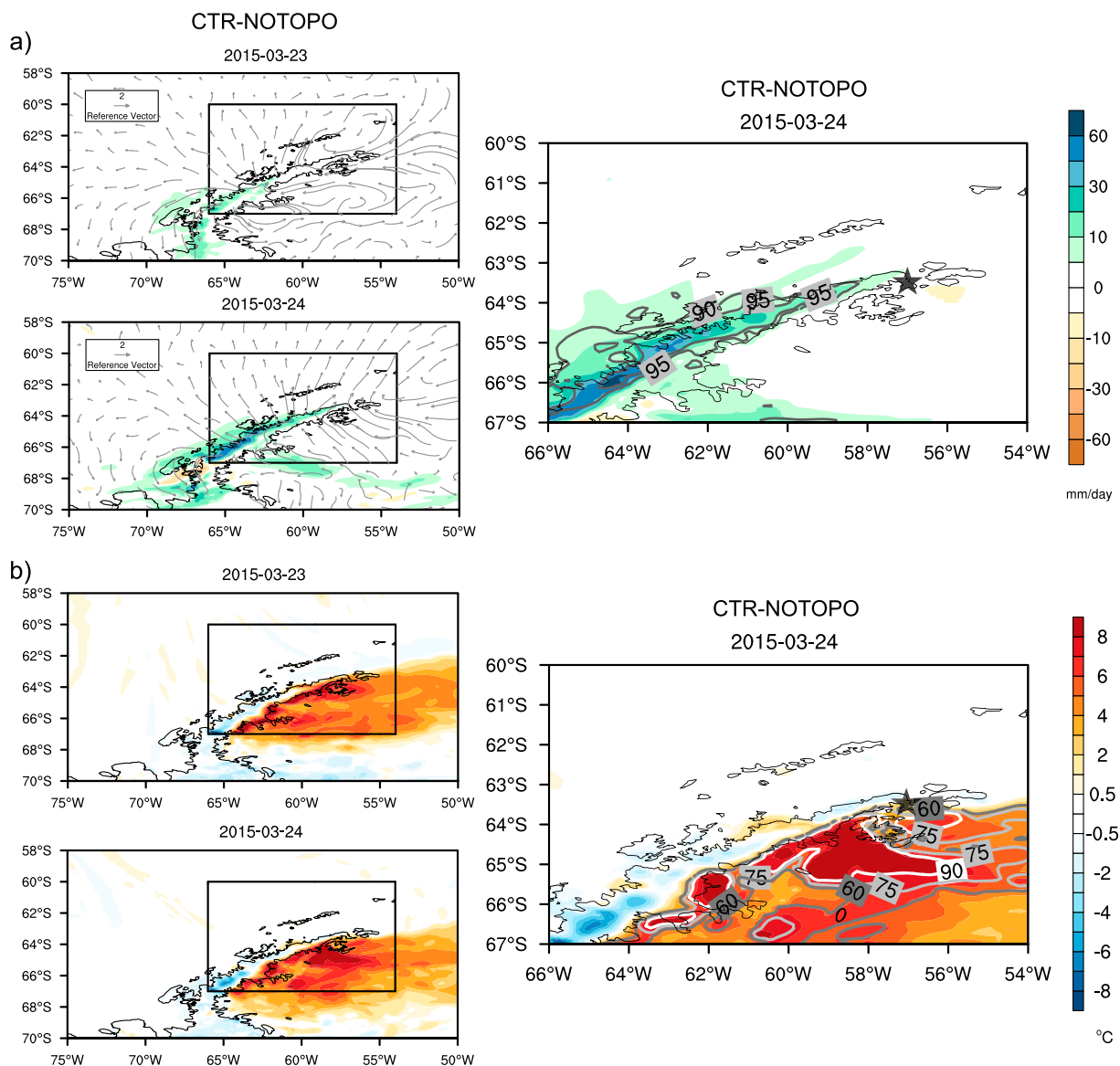


**Figure 13.** (a) Daily precipitation ( $\text{mm d}^{-1}$ ) and 850 hPa wind vector ( $\text{m s}^{-1}$  differences between the CTR and NOTOPO experiments on 23 and 24 March 2015. (b) Same as in (a) but for the daily maximum near-surface air temperature differences ( $^{\circ}\text{C}$ ). The zoom plots on the right show the differences on 24 March 2015 within the rectangular box corresponding to the region where surface topography is removed in the NOTOPO experiment. Black stars show the location of the Esperanza station. Precipitation difference contours correspond to the relative precipitation changes (%) between the CTR and NOTOPO experiments. Temperature difference contours indicate the ratio ( $\times 100$ ) of differences in maximum near-surface air temperature between the CTR and NOTOPO experiments to the ERAINT maximum near-surface air temperature anomalies on 24 March with respect to 1979–2014 climatology (white contours  $>90\%$ , light gray contours  $>75\%$ , and dark gray contours  $>60\%$ ).

experiment. For instance, there are marked differences in wind speed ( $\sim -10 \text{ m s}^{-1}$ ) and air temperature ( $\sim -8^{\circ}\text{C}$ ) at low levels with respect to their CTR counterparts on the leeward side ( $\sim -58.37^{\circ}\text{W}$ ) (Figure 12c). Finally, differences are shown in precipitation, 850 hPa wind vectors, and daily maximum SAT on 23 and 24 March, between the CTR and NOTOPO experiments (Figure 13). Low-level wind vectors around the AP change from CTR to NOTOPO simulations. For instance, CTR-NOTOPO shows an anticyclonic circulation (in other words a cyclonic circulation in NOTOPO) on the windward side of the AP that is very close to the intersection point between the prescribed and the removed topography (Figure 13a). It could be argued that a sharp change in topography could lead to the acceleration of the flow across the northern AP, compared to the rest of the AP, where the foehn effect remains, and hence, a cyclonic vorticity is generated by horizontal shear in NOTOPO.

The CTR-NOTOPO also illustrates that almost all of the precipitation occurs due to the orographic enhancement (e.g., >95% on the windward side of the AP). It is interesting to note that the decreased northwesterly flow due to the anticyclonic circulation on the windward side of the AP results in a decrease in low-level humidity in CTR, with respect to its NOTOPO counterpart over the southern part of the AP (see Figure S12).

Given the fact that the NOTOPO experiment only includes the removal of surface topography in the northern AP, large-scale SAT differences between CTR and NOTOPO are minor on the windward side, indicating little difference in upwind conditions between the two experiments (Figure 13b). However, CTR-NOTOPO shows the existence of local topographically induced warming along the eastern coast of the AP. For instance, a marked warming (>8°C) with respect to NOTOPO occurs on the leeward side of the central AP (around 64°S) on 24 March. As the northern tip of the AP is located away from the main AP mountain range, topographically induced warming on its leeward side is relatively smaller than that in the central AP. As noted before, the CTR experiment has difficulty in reproducing the sudden nature of foehn wind effects at point observations (i.e., Esperanza station), and thus, it underestimates the maximum temperature during the foehn event (see supporting information Text S2). For that reason, rather than attributing the grid-based SAT differences between CTR and NOTOPO ( $\Delta SAT$ ) to the point observation anomalies, we use ERAINT SAT anomalies (with respect to 1979–2014 climatology, see section 2.3) to obtain a grid-based attribution on the leeward side of the AP. A ratio of  $\Delta SAT$  to ERAINT SAT anomalies on 24 March indicates that more than 90% of the warming can be attributed to the foehn effect on the leeward side of central AP, whereas ~60% of the warming can be attributed to the foehn effect over the northern tip of the eastern AP (very close to the Esperanza station) (Figure 13b).

## 5. Conclusions and Discussion

A record-setting temperature (17.5°C) occurred on 24 March 2015 at the Esperanza research base, located near the northern tip of the AP. An AR event resulted in warm and moist air advection toward the AP before the record-setting temperature event, eventually triggering a foehn episode on the leeward side of the central and northern AP on 24 March 2015. The event was investigated using surface station data, satellite imagery, reanalysis data, and numerical simulations. Given the observed long-term daily maximum near-SAT value of 0.2°C on 24 March at the Esperanza station, this extreme event resulted in a +17.3°C temperature anomaly relative to the climatology for that day. Other extreme temperatures were also registered by meteorological stations on the windward side (e.g., 10.5°C at the Base San Martin station and 11.3°C at the Base Arturo Prat station), revealing a widespread effect of large-scale warm air advection toward the AP. The MODIS Antarctic Ice Shelf Image Archive of Larsen B provides clear evidence for disintegration and advection of sea ice, as well as the formation of melt ponds on ice sheet surface at the base of the AP mountain range, illustrating a large impact on the cryosphere by this single extreme event.

The synoptic-scale analysis based on the ERAINT reanalysis data shows a deep low-pressure center over the Amundsen-Bellinghshausen Sea and a blocking ridge over the southeast Pacific which provided favorable conditions for the development of an AR with a northwest-southeast orientation, directing warm and moist air toward the AP and triggering a widespread foehn episode (Figure 14). In the context of 35 years of reanalysis data, the record temperature event on the windward side of the AP is characterized by similarly extreme conditions (up to ~24 m s<sup>-1</sup> wind speeds at 850 hPa and 5,500 m geopotential heights at 500 hPa), and thermodynamic conditions (~12°C air temperature anomalies and more than 30 kg m<sup>-1</sup> s<sup>-1</sup> vapor transport at 850 hPa) during the late summer/early fall (JFM) period.

In order to disentangle the role of the large-scale warm air advection versus the local topographically induced warming, we conducted two numerical simulations using the RegCM4 regional atmospheric model at a 10 km spatial resolution, with and without topography (CTR and NOTOPO, respectively) in the northern AP. The model realistically reproduces the main synoptic fields and extreme conditions before and during the event. Despite this reasonable agreement in large-scale forcing, the model illustrates the difficulty in reproducing the steep SAT increase at foehn onset. Similar difficulties persist even with a relatively higher spatial resolution (6 and 2 km) in the numerical experiment carried out with the WRF model.

Due to both an anomalous moisture flux and vertical stability change, the RegCM4 clearly illustrates orographic precipitation enhancement on the windward side of the AP. Temperature differences between the leeward and windward sides of the AP generally tend to increase as the product of normalized dry Froude number and normalized moisture flux increases. This dynamical linkage illustrates the major contribution

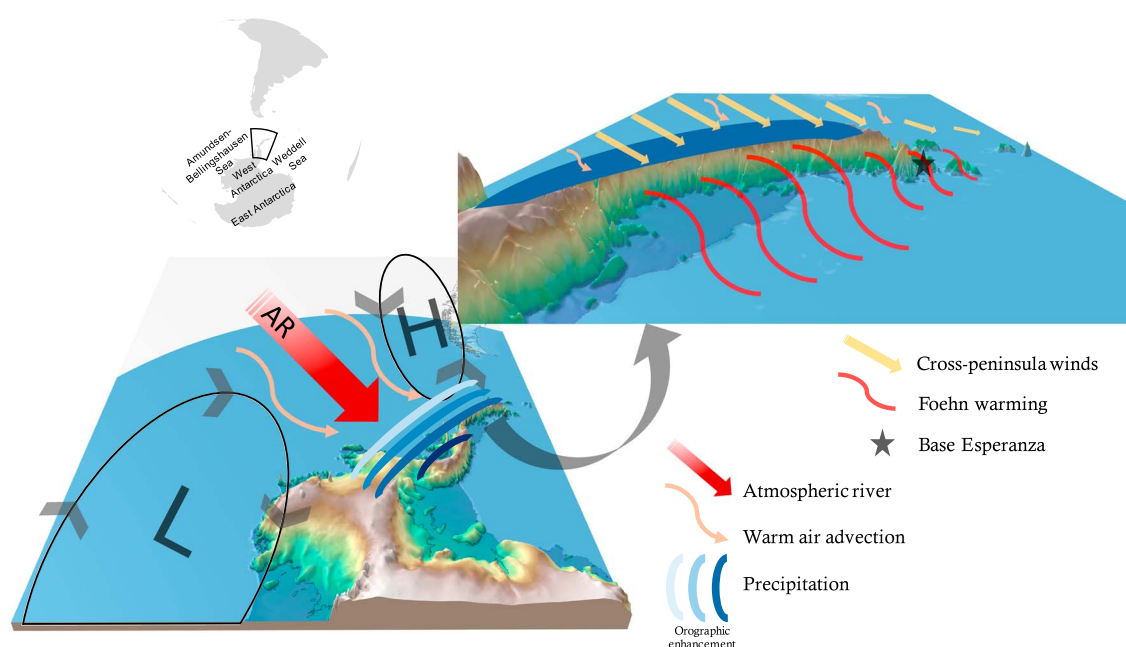


**Figure 14.** A conceptual model of the record-setting temperature occurred on 24 March 2015 at the Esperanza research base on a 3-D view from the south/southeast. The large-scale illustration shows the atmospheric river event (thick red arrow) conditioned by a deep low-pressure center over the Amundsen-Bellinghousen Sea and a northwest-southeast oriented blocking ridge over the southeastern Pacific, directing warm air (thin orange curved arrows) toward the Antarctic Peninsula (AP) from the midlatitudes. Also shown with blue curves, where light to dark blue indicates orographic precipitation enhancement, is precipitation. The illustration, when zoomed in, shows cross-peninsula winds (thick yellow arrows) along the barrier and foehn warming (red curves) along the lee side of the northern AP. Stronger cross-peninsula winds over the highest mountain peaks in the central AP cause more extensive leeside warming, whereas the foehn warming tends to decrease toward the northern tip of the AP, as it is farther away from the main AP mountain range and less exposed to the cross-peninsula winds. AR = atmospheric river.

of the latent heat release, due to orographic precipitation enhancement on the windward side, to foehn warming on the leeward side, which is more pronounced on the leeward side of the central AP when compared to the northern tip. The numerical simulations also indicate the existence of isentropic drawdown of warm air on the leeward side. Temperature difference between CTR and NOTOPO experiments shows the existence of local topographically induced warming along the eastern coast of the AP. Pronounced warming ( $>8^{\circ}\text{C}$ ) with respect to its NOTOPO counterpart occurs on the leeward side of central AP (around  $64^{\circ}\text{S}$ ) on 24 March. Grid points near the Esperanza station indicate relatively smaller warming amplification ( $\sim 2$  to  $6^{\circ}\text{C}$ ) than those in the central AP, as they are located farther away from the main AP mountain range. A grid-to-grid analysis of the warming based on the SAT differences between CTR and NOTOPO simulations and ERAINT SAT anomalies (with respect to the 1979–2014 climatology) indicate that  $>90\%$  of the warming can be attributed to the foehn effect on the leeward side of central AP, whereas  $\sim 60\%$  of the warming can be attributed to the foehn effect for grid points very close to the Esperanza station over the northern tip of eastern AP.

Results presented here suggest a link between local-scale forcing (i.e., foehn effect warming) and large-scale forcing (i.e., AR) in explaining the record-setting temperature occurring on 24 March 2015 at the Esperanza research base. A key finding in our analysis is that the water vapor reaching the windward side of the AP due to the AR was instrumental to the orographic precipitation enhancement and latent heat release on the windward side, suggesting that the main foehn mechanism was at work during this episode. Nevertheless, the foehn effect warming is not uniform along the leeside of the AP, with a more pronounced warming along the eastern side of the central AP. These results confirm the findings of Elvidge et al. (2016), who revealed that stronger cross-peninsula winds over the higher mountain peaks in the central AP cause more extensive leeside warming (Figure 14). As the steep terrain of the AP results in an inadequate representation of the foehn effect warming, particularly over its northern tip, this study and other recent studies (e.g., Elvidge et al., 2015) emphasize the need for further modeling research to better understand the different physical processes during extreme temperature events. Furthermore, the occurrence of these extreme temperature events in the AP opens questions concerning the cause of frequency of such events, as well the role of extreme episodes

versus weaker, long-term temperature trends in the fate of ice sheet surfaces and ice shelves in the eastern side of the AP.

Finally, given the documented potential of ARs to produce high-impact coastal winds and extreme events around the globe (Waliser & Guan, 2017), it can be argued that an anomalous source of water vapor enhancing the moisture transport toward the AP through ARs may play a crucial role in the occurrence of foehn events, as well as in determining the extremity of these events. We highlight that moisture transport is also critical in understanding temperature effects on the surface cryosphere, given the large warming amplification that occurs with this particular event. We have refrained here from dwelling on the origin of the AR and its associated atmospheric teleconnection forcing. Therefore, further research is needed to better clarify the mechanisms at both hemispheric and local scales which control the occurrence of extreme temperature events on the AP.

#### Acknowledgments

This study was supported by FONDAP/CONICYT Chile (grant 15110009-CR2). Deniz Bozkurt acknowledges the Scientific Committee on Antarctic Research (SCAR) for travel funding to the 12th Workshop on Antarctic Meteorology and Climate (WAMC) workshop as well as the Year of Polar Prediction in the Southern Hemisphere (YOPP-SH) meeting at NCAR, Boulder, Colorado, USA, between 26 and 29 June 2017. Deniz Bozkurt also acknowledges David Bromwich and the organizers and participants of the meetings for their valuable feedback on this study. The authors are grateful to the British Antarctic Survey that provides the SCAR meteorological data used in this study. Both surface and upper air data are available at [ftp://ftp.bas.ac.uk/src/SCAR\\_EGOMA/](ftp://ftp.bas.ac.uk/src/SCAR_EGOMA/). The GHCN data are available at the Chilean Climate Explorer's website (<http://explorador.cr2.cl>). The authors appreciate the support of the University of Wisconsin-Madison Antarctic Meteorological Research Center for the data set, data display, and information (NSF grant ANT-1535632, data available at <ftp://amrc.ssec.wisc.edu/archive/2015/>). The authors also are grateful to the National Snow and Ice Data Center (NSIDC) for providing the MODIS Antarctic Ice Shelf Image Archive, available at [https://nsidc.org/data/iceshelves\\_images/](https://nsidc.org/data/iceshelves_images/). We thank Valeria Rudloff for compiling surface precipitation data over Antarctica. Deniz Bozkurt benefited from useful discussions with Maximiliano Viale on atmospheric rivers, blocking, and stability. Deniz Bozkurt also thanks to Eurasia Institute of Earth Sciences and Polar Research Center at Istanbul Technical University for their logistical support during the visit to Turkey. Powered@NLHPC: This research was supported by the supercomputing infrastructure of the NLHPC (ECM-02). We are grateful to Irina Gorodetskaya and two anonymous referees for their constructive and helpful comments which helped to improve the manuscript.

#### List of Abbreviations

AMRC	= The University of Wisconsin-Madison Antarctic Meteorological Research Center
AP	= The Antarctic Peninsula
CTR	= A control simulation that used the default topographic features
ECMWF	= The European Centre for Medium-Range Weather Forecasts
ERAINT	= A global atmospheric reanalysis of ECMWF from 1979, continuously updated in real time
JFM	= January-February-March
GDAS	= The Global Data Assimilation System
GHCN	= The Global Historical Climatology Network
IVT	= Integrated vapor transport
IWV	= Integrated water vapor
MODIS	= The Moderate Resolution Imaging Spectroradiometer
NE-SW	= Northeast-southwest
NOTOPO	= A topography removal simulation that removes the surface topography
NSIDC	= The National Snow and Ice Data Center
RCM	= Regional climate model
RegCM4	= The Abdus Salam International Centre for Theoretical Physics Regional Climate Model (v4)
SAM	= The Southern Annular Mode
SAT	= Near-surface air temperature
SCAR	= The Scientific Committee for Antarctic Research
UTC	= Coordinated Universal Time
VT	= Vapor transport
WMO-CCI	= The World Meteorological Organization Commission for Climatology
WRF	= The Weather and Research Forecast Model

#### References

- American Meteorological Society (2017). Atmospheric river, American Meteorological Society. Retrieved from [http://glossary.ametsoc.org/wiki/Atmospheric\\_river](http://glossary.ametsoc.org/wiki/Atmospheric_river)
- Anthes, R. A. (1977). A cumulus parameterization scheme utilizing a one-dimensional cloud model. *Monthly Weather Review*, *105*, 270–286.
- Ashmore, D. W., Hubbard, B., Luckman, A., Kulesa, B., Bevan, S., Booth, A., et al. (2017). Ice and firn heterogeneity within Larsen C Ice Shelf from borehole optical televiewing. *Journal of Geophysical Research: Earth Surface*, *122*, 1139–1153. <https://doi.org/10.1002/2016JF004047>
- Barrett, B. S., Campos, D. A., Veloso, J. V., & Rondanelli, R. (2016). Extreme temperature and precipitation events in March 2015 in central and northern Chile. *Journal of Geophysical Research: Atmospheres*, *121*, 4563–4580. <https://doi.org/10.1002/2016JD024835>
- Bindschadler, R., Vornberger, P., Fleming, A., Fox, A., Mullins, J., Binnie, D., et al. (2008). The Landsat image mosaic of Antarctica. *Remote Sensing of Environment*, *112*(12), 4214–4226.
- Bozkurt, D., Rondanelli, R., Garreaud, R., & Arriagada, A. (2016). Impact of warmer eastern tropical Pacific SST on the March 2015 Atacama floods. *Monthly Weather Review*, *144*(11), 4441–4460.
- Brinkmann, W. A. R. (1971). What is a foehn? *Weather*, *26*, 230–239.
- Cape, R. M., Vernet, M., Kahru, M., & Spreen, G. (2014). Polynya dynamics drive primary production in the Larsen A and B embayments following ice shelf collapse. *Journal of Geophysical Research: Oceans*, *119*, 572–594. <https://doi.org/10.1002/2013JC009441>
- Cape, M. R., Vernet, M., Skvarca, P., Marinsek, S., Scambos, M., & Domack, E. (2015). Foehn winds link climate-driven warming to ice shelf evolution in Antarctica. *Journal of Geophysical Research: Atmospheres*, *120*, 11,037–11,057. <https://doi.org/10.1002/2015JD023465>
- Carrasco, J. F. (2013). Decadal changes in the near-surface air temperature in the western side of the Antarctic Peninsula. *Atmospheric and Climate Sciences*, *3*, 275–281.

- Cofaigh, C. O., Davies, B. J., Livingstone, S. J., Smith, J. A., Johnson, J. S., Hocking, E. P., et al. (2014). Reconstruction of ice-sheet changes in the Antarctic Peninsula since the Last Glacial Maximum. *Quaternary Science Reviews*, *100*, 87–110. <https://doi.org/10.1016/j.quascirev.2014.06.023>
- Convey, P., & Smith, R. I. L. (2006). Responses of terrestrial Antarctic ecosystems to climate change. *Plant Ecology*, *182*(1–2), 1–10.
- Cook, A. J., & Vaughan, D. G. (2010). Overview of areal changes of the ice shelves on the Antarctic Peninsula over the past 50 years. *Cryosphere*, *4*(1), 77–98. <https://doi.org/10.5194/tc-4-77-2010>
- Cook, A. J., Fox, A. J., Vaughan, D. G., & Ferrigno, J. G. (2005). Retreating glacier fronts on the Antarctic Peninsula over the past half-century. *Science*, *308*, 541–544.
- Dee, D. P., Uppala, S. M., Berrisford, P., Poli, P., Kobayashi, S., Andrae, U., et al. (2011). The ERA-Interim reanalysis: Configuration and performance of the data assimilation system. *Quarterly Journal of the Royal Meteorological Society*, *137*, 553–597.
- Dettinger, M. D., Ralph, F. M., Das, T., Neiman, P. J., & Cayan, D. R. (2011). Atmospheric rivers, floods and the water resources of California. *Water*, *3*(4), 445–478.
- Dickinson, R. E., Henderson-Sellers, A., & Kennedy, P. J. (1993). Biosphere-atmosphere transfer scheme (BATS) Version 1e as coupled to the NCAR Community Climate Model (NCAR Tech. Note NCAR/TN-387+STR). NCAR: Boulder.
- Elvidge, A. D., & Renfrew, I. A. (2016). The causes of foehn warming in the lee of mountains. *Bulletin of the American Meteorological Society*, *97*, 455–466. <https://doi.org/10.1175/BAMS-D-14-00194.1>
- Elvidge, A. D., Renfrew, I. A., King, J. C., Orr, A., & Lachlan-Cope, T. A. (2016). Foehn warming distributions in nonlinear and linear flow regimes: A focus on the Antarctic Peninsula. *Quarterly Journal of the Royal Meteorological Society*, *142*, 618–631. <https://doi.org/10.1002/qj.2489>
- Elvidge, A. D., Renfrew, I. A., King, J. C., Orr, A., Lachlan-Cope, T. A., Weeks, M., et al. (2015). Foehn jets over the Larsen C Ice Shelf, Antarctica. *Quarterly Journal of the Royal Meteorological Society*, *141*, 698–713. <https://doi.org/10.1002/qj.2382>
- Emanuel, K. A. (1991). A scheme for representing cumulus convection in large-scale models. *Journal of the Atmospheric Sciences*, *48*, 2313–2335.
- ETOPO2v2 (2006). *2-minute gridded global relief data*. National Geophysical Data Center, NOAA. Retrieved from <https://www.ngdc.noaa.gov/mgg/global/relief/ETOPO2/ETOPO2v2-2006/>
- Gimeno, L., Nieto, R., Vázquez, M., & Lavers, D. A. (2014). Atmospheric rivers: A mini-review. *Frontiers in Earth Science*, *2*, 2.
- Giorgi, F., Marinucci, M. R., & Bates, G. T. (1993). Development of a second generation regional climate model (RegCM2). Part I: Boundary layer and radiative transfer processes. *Monthly Weather Review*, *121*, 2794–2813. [https://doi.org/10.1175/1520-0493\(1993\)121<2794:DOASGR>2.0.CO;2](https://doi.org/10.1175/1520-0493(1993)121<2794:DOASGR>2.0.CO;2)
- Giorgi, F., Marinucci, M. R., Bates, G. T., & DeCanio, G. (1993). Development of a second generation regional climate model (RegCM2). Part II: Convective processes and assimilation of lateral boundary conditions. *Monthly Weather Review*, *121*, 2814–2832. [https://doi.org/10.1175/1520-0493\(1993\)121<2814:DOASGR>2.0.CO;2](https://doi.org/10.1175/1520-0493(1993)121<2814:DOASGR>2.0.CO;2)
- Giorgi, F., Coppola, E., Solmon, F., Mariotti, L., Sylla, M. B., Bi, X., et al. (2012). RegCM4: Model description and preliminary tests over multiple CORDEX domains. *Climate Research*, *52*, 7–29. <https://doi.org/10.3354/cr01018>
- Giorgi, F., Torma, C., Coppola, E., Ban, N., Schar, C., & Somot, S. (2016). Enhanced summer convective rainfall at Alpine high elevations in response to climate warming. *Nature Geoscience*, *9*, 584–589. <https://doi.org/10.1038/ngeo2761>
- Gorodetskaya, I. V., Tsukernik, M., Claes, K., Ralph, M. F., Neff, W. D., & Van Lipzig, P. M. (2014). The role of atmospheric rivers in anomalous snow accumulation in East Antarctica. *Geophysical Research Letters*, *41*, 6199–6206. <https://doi.org/10.1002/2014GL060881>
- Grassi, B., Redaelli, G., & Visconti, G. (2013). Arctic sea ice reduction and extreme climate events over the Mediterranean region. *Journal of Climate*, *26*, 10,101–10,110.
- Grell, G. A. (1993). Prognostic evaluation of assumptions used by cumulus parameterizations. *Monthly Weather Review*, *121*, 764–787.
- Grell, G. A., Dudhia, J., & Stauffer, D. R. (1994). Description of the fifth generation Penn State/NCAR Mesoscale Model (MM5) (NCAR Tech. Note NCAR/TN-398+STR). Boulder, CO: NCAR.
- Holtzlag, A. A. M., de Bruijn, E. I. F., & Pan, H. L. (1990). A high resolution air mass transformation model for short-range weather forecasting. *Monthly Weather Review*, *118*, 1561–1575. [https://doi.org/10.1175/1520-0493\(1990\)118<1561:AHRAMT>2.0.CO;2](https://doi.org/10.1175/1520-0493(1990)118<1561:AHRAMT>2.0.CO;2)
- Hong, S. Y., & Lim, J. O. (2006). The WRF single-moment 6-class microphysics scheme (WSM6). *Journal of the Korean Meteorological Society*, *42*, 129–151.
- Kiehl, J. T., Hack, J. J., Bonan, G. B., Boville, B. A., Breigleb, B. P., Williamson, D., et al. (1996). Description of the NCAR Community Climate Model (CCM3) (NCAR Tech. Note NCAR/TN-420+STR). Boulder, CO: NCAR.
- King, J. C., & Turner, J. (2009). *Antarctic meteorology and climatology*. Cambridge, UK: Cambridge University Press. <https://doi.org/10.1017/CBO9780511524967>
- Kunz, M., & Wassermann, S. (2011). Sensitivity of flow dynamics and orographic precipitation to changing ambient conditions in idealised model simulations. *Meteorologische Zeitschrift*, *20*, 199–215. <https://doi.org/10.1127/0941-2948/2011/0221>
- Kushner, P. J., Held, I. M., & Delworth, T. L. (2001). Southern Hemisphere atmospheric circulation response to global warming. *Journal of Climate*, *14*, 2238–2249.
- Main, J. S. (2004). The Kain-Fritsch convective parameterization: An update. *Journal of Applied Meteorology and Climatology*, *43*, 170–181.
- Marshall, G. J., Orr, A., van Lipzig, N. P. M., & King, J. C. (2006). The impact of a changing Southern Hemisphere annular mode on Antarctic Peninsula summer temperatures. *Journal of Climate*, *19*(20), 5388–5404. <https://doi.org/10.1175/JCLI3844.1>
- Menne, M. J., Durre, I., Vose, R. S., Gleason, B. E., & Houston, T. G. (2012). An overview of the Global Historical Climatology Network-Daily Database. *Journal of Atmospheric and Oceanic Technology*, *29*, 897–910. <https://doi.org/10.1175/JTECH-D-11-00103.1>
- Mlawer, E. J., Taubman, S. J., Brown, P. D., Iacono, M. J., & Clough, S. A. (1997). Radiative transfer for inhomogeneous atmosphere: RRTM, a validated correlated-k model for the longwave. *Journal of Geophysical Research*, *102*, 16,663–16,682.
- Montes-Hugo, M., Doney, S. C., Ducklow, H. W., Fraser, W., Martinson, D., Stammerjohn, S. E., et al. (2009). Recent changes in phytoplankton communities associated with rapid regional climate change along the western Antarctic Peninsula. *Science*, *323*(5920), 1470–1473. <https://doi.org/10.1126/science.1164533>
- Nakanishi, M., & Niino, H. (2006). An improved Mellor-Yamada Level-3 model: Its numerical stability and application to a regional prediction of advection fog. *Boundary-Layer Meteorology*, *119*, 397–407.
- Nicolas, J. P., Vogelmann, A. M., Scott, R. C., Wilson, A. B., Cadeddu, M. P., Bromwich, D. H., et al. (2017). January 2016 extensive summer melt in West Antarctica favoured by strong El Niño. *Nature Communications*, *8*, 15799. <https://doi.org/10.1038/ncomms15799>
- Oliva, M., Navarro, F., Hrbacek, F., Hernandez, A., Nyvlt, D., Pereira, P., et al. (2017). Recent regional climate cooling on the Antarctic Peninsula and associated impacts on the cryosphere. *Science of the Total Environment*, *580*, 210–223. <https://doi.org/10.1016/j.scitotenv.2016.12.030>

- Pal, J. S., Giorgi, F., Bi, X., Elguindi, N., Solmon, F., Gao, X., et al. (2007). Regional climate modeling for the developing world: The ICTP RegCM3 and RegCNET. *Bulletin of the American Meteorological Society*, *88*, 1395–1409. <https://doi.org/10.1175/BAMS-88-9-1395>
- Pal, J. S., Small, E. E., & Eltahir, E. A. B. (2000). Simulation of regional-scale water and energy budgets: Representation of surged cloud and precipitation processes within RegCM. *Journal of Geophysical Research*, *105*, 29,579–29,594.
- Pritchard, H. D., & Vaughan, D. G. (2007). Widespread acceleration of tidewater glaciers on the Antarctic Peninsula. *Journal of Geophysical Research*, *112*, F03S29. <https://doi.org/10.1029/2006JF000597>
- Ralph, F. M., Neiman, P. J., & Wick, G. A. (2004). Satellite and CALJET aircraft observations of atmospheric rivers over the Eastern North Pacific Ocean during the winter of 1997/98. *Monthly Weather Review*, *132*, 1721–1745.
- Reynolds, R. W., Rayner, N. A., Smith, T. M., Stokes, D. C., & Wang, W. (2002). An improved in situ and satellite SST analysis for climate. *Journal of Climate*, *15*, 1609–1625.
- Rignot, E., Casassa, G., Gogineni, P., Krabill, W., Rivera, A., & Thomas, R. (2004). Accelerated ice discharge from the Antarctic Peninsula following the collapse of Larsen B Ice Shelf. *Geophysical Research Letters*, *31*, L18401. <https://doi.org/10.1029/2004GL020697>
- Scambos, T., Bohlander, J., & Raup, B. (1996). Images of Antarctic Ice Shelves, Larsen B Ice Shelf, National Snow and Ice Data Center. Retrieved from [https://nsidc.org/data/iceshelves\\_images/index\\_modis.html](https://nsidc.org/data/iceshelves_images/index_modis.html)
- Scambos, T. A., Bohlander, J. A., Human, C. A., & Skvarca, P. (2004). Glacier acceleration and thinning after ice shelf collapse in the Larsen B embayment. *Geophysical Research Letters*, *31*, L18402. <https://doi.org/10.1029/2004GL020670>
- Schlosser, E. K., Manning, W., Powers, J. G., Duda, M. G., Birnbaum, G., & Fujita, K. (2014). Characteristics of high precipitation events in Dronning Maud Land, Antarctica. *Journal of Geophysical Research: Atmospheres*, *115*, D14107. <https://doi.org/10.1029/2009JD013410>
- Schofield, O., Ducklow, H. W., Martinson, D. G., Meredith, M. P., Moline, W., & Fraser, M. A. (2010). How do polar marine ecosystems respond to rapid climate change? *Science*, *328*(5985), 1520–1523. <https://doi.org/10.1126/science.1185779>
- Shindell, D. T., & Schmidt, G. A. (2004). Southern Hemisphere climate response to ozone changes and greenhouse gas increases. *Geophysical Research Letters*, *31*, L18209. <https://doi.org/10.1029/2004GL020724>
- Skamarock, W. C., Klemp, J. B., Dudhia, J., Gill, D. O., Barker, D. M., Duda, M. G., et al. (2008). A description of the advanced research WRF version 3 (NCAR Tech. Note NCAR/TN-475+ST). Boulder, CO: NCAR.
- Skansi, M. L. M., King, J., Lazzara, M. A., Cerveny, R. S., Stella, J. L., Solomon, S., et al. (2017). Evaluating highest-temperature extremes in the Antarctic. *EOS*, *98*. <https://doi.org/10.1029/2017EO068325>
- Speirs, J. C., McGowan, H. A., Steinhoff, D. F., & Bromwich, D. H. (2013). Regional climate variability driven by foehn winds in the McMurdo Dry Valleys, Antarctica. *International Journal of Climatology*, *33*, 945–958.
- Speirs, J. C., Steinhoff, D. F., McGowan, H. A., Bromwich, D. H., & Monaghan, A. J. (2010). Foehn winds in the McMurdo Dry Valleys, Antarctica: The origin of extreme warming events. *Journal of Climate*, *23*, 3577–3598.
- Turner, J., Lu, H., White, I., King, J. C., Phillips, T., Hosking, J. S., et al. (2016). Absence of 21st century warming on Antarctic Peninsula consistent with natural variability. *Nature*, *535*, 411–415. <https://doi.org/10.1038/nature18645>
- Uotila, P., Vihma, T., & Tsukernik, M. (2013). Close interactions between the Antarctic cyclone budget and large-scale atmospheric circulation. *Geophysical Research Letters*, *40*, 3237–3241. <https://doi.org/10.1002/grl.50560>
- van Wessem, J. M., Reijmer, C. H., Morlighem, M., Mouginit, J., Rignot, E., Medley, B., et al. (2014). Improved representation of East Antarctic surface mass balance in a regional atmospheric climate model. *Journal of Glaciology*, *60*, 761–770.
- van Wessem, J. M., Reijmer, C. H., van de Berg, W. J., & van den Broeke, M. R. (2015). Temperature and wind climate of the Antarctic Peninsula as simulated by a high-resolution regional atmospheric climate model. *Journal of Climate*, *28*, 7306–7326.
- Viale, M., & Nuñez, M. (2011). Climatology of winter orographic precipitation over the subtropical Central Andes and associated synoptic and regional characteristics. *Journal of Hydrometeorology*, *12*(4), 481–507.
- Voosen, P. (2017). *Delaware-sized iceberg splits from Antarctica*. Science-AAAS. Retrieved from <http://www.sciencemag.org/news/2017/07/delaware-sized-iceberg-splits-antarctica>
- Waliser, D., & Guan, B. (2017). Extreme winds and precipitation during landfall of atmospheric rivers. *Nature Geoscience*, *10*, 179–183. <https://doi.org/10.1038/ngeo2894>
- Zeng, X., Zhao, M., & Dickinson, R. E. (1998). Intercomparison of bulk aerodynamic algorithms for the computation of sea surface fluxes using TOGA COARE and TAO data. *Journal of Climate*, *11*, 2628–2644. [https://doi.org/10.1175/1520-0442\(1998\)011<2628:IOBAAF>2.0.CO;2](https://doi.org/10.1175/1520-0442(1998)011<2628:IOBAAF>2.0.CO;2)